

**UCLA**

**UCLA Electronic Theses and Dissertations**

**Title**

Modeling and Validation of Coastal Wastewater Effluent Plumes Using High-Resolution Nonhydrostatic Regional Ocean Modeling System

**Permalink**

<https://escholarship.org/uc/item/5ht6r7cf>

**Author**

Ho, Minna

**Publication Date**

2019

Peer reviewed|Thesis/dissertation

UNIVERSITY OF CALIFORNIA

Los Angeles

Modeling and Validation of  
Coastal Wastewater Effluent Plumes Using High-Resolution  
Nonhydrostatic Regional Ocean Modeling System

A thesis submitted in partial satisfaction  
of the requirements for the degree  
Master of Science in Civil Engineering

by

Minna Ho

2019

© Copyright by

Minna Ho

2019

# ABSTRACT OF THE THESIS

## Modeling and Validation of Coastal Wastewater Effluent Plumes Using High-Resolution Nonhydrostatic Regional Ocean Modeling System

by

Minna Ho

Master of Science in Civil Engineering

University of California, Los Angeles, 2019

Professor Timu Gallien, Chair

A wastewater pipe module is developed and implemented into a high-resolution, nonhydrostatic circulation model, the Regional Ocean Modeling System (ROMS). Intermediate and far field dilution and plume rise height is validated to cross flow laboratory experiments of Roberts, Snyder, and Baumgartner. The domain and diffuser is modeled after Southern California Bight (SCB) discharge regions with idealized flat bottom topography, linearly density-stratified vertical profile, and uniform current to mimic laboratory setup in a scaled-up domain. Direct Froude number comparisons are made. Buoyant plume flow regimes are accurately reproduced, and dilution metrics are reasonably predicted for low Froude numbers (i.e.,  $F \leq 1$ ). High Froude numbers require more distance away from pipe for accurate plume characteristics. Generally, low cross flow velocity simulations, consistent with typical SCB coastal currents, are reasonably well-resolved using the 3 meter nonhydrostatic ROMS model. High Froude number flows may require effluent input parameterization adjustment or additional spatial resolution.

The thesis of Minna Ho is approved.

Michael K. Stenstrom

Daniele Bianchi

Timu Gallien, Committee Chair

University of California, Los Angeles

2019

## TABLE OF CONTENTS

<b>1</b>	<b>Introduction</b>	<b>1</b>
1.1	Effluent Discharge in the Coastal Ocean	1
1.2	Near and Intermediate Field Modeling	4
1.2.1	Analytical and Empirical Models	5
1.2.2	Jet Integral Method	8
1.3	Far field Modeling	14
1.3.1	Lagrangian Plume Dispersion Modeling	14
1.3.2	Eulerian Modeling	15
<b>2</b>	<b>Modeling Approach</b>	<b>19</b>
2.1	High-Resolution Nonhydrostatic ROMS Model	19
2.1.1	Hydrostatic versus Nonhydrostatic	21
2.2	Validation Data	23
2.3	ROMS Plume Modeling	24
2.3.1	Model Grid	24
2.3.2	Diffuser Representation and Effluent Flux Forcing	25
2.3.3	High-Resolution Nonhydrostatic ROMS Validation Experiments	28
2.3.4	Ambient Stratification	29
<b>3</b>	<b>Results</b>	<b>32</b>
3.1	ROMS RSB Validation Experiments	32
3.2	Sensitivity to resolution	42
3.3	Sensitivity to time step	48

<b>4</b>	<b>Discussion</b>	<b>52</b>
4.1	Minimum Dilution Height	52
4.2	Realistic Stratification	54
4.3	Resolution	56
4.4	High Froude Number Instability	57
<b>5</b>	<b>Conclusions and Future Work</b>	<b>58</b>

## LIST OF FIGURES

1.1	Location of all wastewater treatment plants that discharge into the Southern California Bight. Red dots indicate major dischargers and purple triangles indicate minor dischargers. . . . .	2
1.2	Laboratory simulation of a single port issuing a buoyant jet horizontally. Adapted from Koh and Brooks, 1975. . . . .	3
1.3	Physical processes of discharged submerged wastewater and corresponding length and time scales. Adapted from Niu et al., 2011; Jirka et al., 1975. . . . .	4
1.4	Diagram of observed characteristics of a multiport diffuser adapted from Roberts et al., 1989a. . . . .	8
1.5	Lagrangian plume element at three stages of development indicated by black bars. (a) side view, and (b) oblique. Adapted from Frick et al., 1994. . . . .	11
1.6	Conceptual diagram of using a near field jet integral model to initialize a Lagrangian RWPT model. Adapted from Kim et al., 2002. . . . .	17
2.1	Instantaneous fields of ROMS zero current plume simulations at 10 meter horizontal resolution with hydrostatic approximation on (a), and off (b). The plume is excessively buoyant and overly diffused in the hydrostatic simulation. Plume is represented by a passive tracer, tpas. KPP turbulence closure is present in the hydrostatic model and not present in the nonhydrostatic. . . . .	23
2.2	Schematic of RSB experimental configuration adapted from Roberts et al., 1989a. Tow tank was 25 meters long, 1.2 meters deep, and 2.4 meters wide. . . . .	24
2.3	Representation of OCSD pipes. Black lines are bathymetry contours and brown lines are OCSD pipe. The pipe in regular use is the 120-inch outfall and is often called the “5-mile pipe”. The shorter 78-inch outfall is used only in emergency situations and during diversions for maintenance on the 5-mile pipe. Red circle is idealized pipe modeled in this study. Adapted from Rogowski et al., 2014. . .	27

2.4	ROMS vertical temperature, salinity, and resultant density profile implemented across the horizontal domain of the simulations. . . . .	31
3.1	Instantaneous concentration fields of ROMS experiments $F = 0, 0.1, 1, 10, 100$ after 11.5 hours from the center of pipe to the eastern boundary. Note only the right side of the domain of $F = 0$ plume is shown with a smaller domain. . . . .	33
3.2	Minimum dilutions for each Froude number at normalized distances away from the pipe. Solid lines are ROMS experiments for each Froude number. Symbols are RSB experiments, and red dashed line is Equation 3.1 representing location of established wastefield in RSB experiments. Navy dashed line intersects points of established wastefield in ROMS experiments. . . . .	35
3.3	Normalized minimum dilution in the established wastefield for each Froude number.	37
3.4	Normalized height to minimum dilution in the established wastefield for each Froude number. . . . .	38
3.5	Height to top of the established wastefield, defined as 5% of maximum concentration, for each Froude number. . . . .	40
3.6	Thickness of the established wastefield, defined as 5% of maximum concentration, for each Froude number. . . . .	41
3.7	Height to minimum dilution at normalized distances away from the pipe. This metric was not presented by Roberts et al., 1989a,b,c. . . . .	42
3.8	Snapshots of passive tracer at (a) 1 m resolution, (b) 3 m resolution, and (c) 10 m resolution with $F = 100$ at the center of the pipe length and after 11.75 hours of model time. Note different $x$ -scale for (a) compared to (b) and (c). . . . .	43
3.9	As 3.2, minimum dilutions over distance away from the pipe with solely Froude number 100 experiments with original 3 m resolution, 1 m resolution (gray), 10 m resolution (brown), and halved pipe source width (yellow). Navy dashed line is updated ROMS established wastefield curve with dilution in the 1 m resolution.	44

3.10	As Figure 3.3, minimum dilution in the established wastefield for each Froude number at different resolutions for $F = 100$ experiments. Gray symbol represents 1 m resolution run, brown symbol represents 10 m resolution, and yellow represents smaller source width. . . . .	45
3.11	As Figure 3.4, height to minimum dilution in the established wastefield for each Froude number. . . . .	46
3.12	Height to top of the established wastefield, defined as 5% of maximum concentration, for each Froude number including additional $F = 100$ simulations. . . .	47
3.13	Thickness of the established wastefield, defined as 5% of maximum concentration, for each Froude number including additional $F = 100$ ROMS experiments. . . .	47
3.14	Instantaneous fields of passive tracer in $F = 10$ experiments with time steps of 2, 2.5, and 3 seconds after 2.25 hours of simulation time. Snapshot is taken at the middle of the length of the pipe. . . . .	48
3.15	Vertical profiles of Froude number 10 experiments at different time steps examining $w$ , $u$ , and passive tracer concentration with time steps in seconds. Note that $dt = 1, 1.5, 2,$ and $2.5$ profile lines are on top of each other . . . . .	49
3.16	Comparison of different time stepping values for $F = 1$ case of vertical velocity $w$ , cross flow velocity $u$ , and passive tracer concentration $tpas$ vertical profiles averaged over length of the pipe and 700 – 1.3 km away from the pipe. . . . .	50
3.17	Vertical velocities comparison of $F = 1$ simulations at different time steps averaged in along pipe distance and over the first 5.75 hours. Top plot is $dt = 3$ seconds and bottom is $dt = 1.5$ seconds. . . . .	51
4.1	Simple density calculation to determine height in meters to neutral buoyancy. Blue line is initial ambient density profile from Figure 2.4, and symbols represent the height to neutral buoyancy of minimum dilution for each Froude number experiment. . . . .	53

4.2	Observed ocean profile from CTD instrument measurement (red) plotted next to the average of all observation profiles within a 3 by 3 km area of the pipe (green) the linear profile (blue) used in these ROMS simulations. . . . .	55
4.3	Neutral density calculation comparing linear and single observation profile. . . . .	56

## LIST OF TABLES

2.1	ROMS experimental parameters. For all experiments, buoyancy frequency $N = 0.010997 \text{ s}^{-1}$ and buoyancy flux $b = 0.00298 \text{ m}^3 \text{ s}^{-3}$ . . . . .	30
3.1	Percent difference between ROMS simulation data and closest RSB series 3 and 4 experiments. Negative percentages indicate underprediction and positive percentages indicate overprediction. . . . .	34

## ACKNOWLEDGMENTS

This work would not have been possible without the financial support of the Southern California Coastal Water Research Project and the Orange County Sanitation District. I would like to thank all the people that guided me in this research endeavor for their continued encouragement and advice.

My deep gratitude extends to Professor Timu Gallien for her patient guidance, constructive suggestions, and instillation of scientific pursuit. I would also like to express my great appreciation to Dr. Jeroen Molemaker for his close collaboration, continuous discussion on this research topic, and his advice in pursuing scientific careers. My grateful thanks are also extended to Professor Daniele Bianchi for integrating me into his group and consistent encouragement, to Professor Michael K. Stentrom for his understanding and advice, Professor Jim McWilliams for his broad-scale advice and use of his facilities, to Dr. Faycal Kessouri and Dr. Martha Sutula for constant scientific support and mentoring, to George Robertson for his cooperation and constructive recommendations, to the members of the modeling team in Center for Earth Systems Research for welcoming me and assisting whenever asked, and to my peers in graduate school for their enthusiasm in support.

Finally, I wish to thank my family and friends for their moral support and encouragement.

# CHAPTER 1

## Introduction

### 1.1 Effluent Discharge in the Coastal Ocean

Marine outfalls discharge municipal wastewater into coastal environments. There are 17 wastewater treatment plants in the Southern California Bight (SCB) that discharge 1.5B L day<sup>-1</sup> of treated wastewater to the ocean (Schiff et al., 2016). In 2000, the four largest publicly owned treatment works (POTWs), Hyperion Treatment Plant (HTP), Joint Water Pollution Control Plant (JWPCP), Orange County Sanitation District (OCSD), and Point Loma Wastewater Treatment Plant (PLWTP), represented 95% of all regional wastewater flows (Schiff et al., 2000). Figure 1.1 shows all SCB POTWs. Since the passing of the Clean Water Act, effluent volumes have decreased by 10%, and contaminant loads have been reduced by more than 90% in the last 50 years despite more than a doubling of population (Lyon and Stein, 2008).

Howard et al., 2014 reported that wastewater discharge contributes similar quantities of nitrogen as wind-driven upwelling in most subregions within 20 kilometers of the coast in the SCB. Wastewater effluent nitrification rate on average is about 80 nmol L<sup>-1</sup> d<sup>-1</sup>. Discharged wastewater has been shown to be a significant ‘new’ nitrate source available in SCB marine environments with nitrification rates increasing up to three-fold due to the presence of wastewater ammonium (McLaughlin et al., 2017). ‘Hot spots’ of remotely sensed surface chlorophyll concentrations, which indicate increased primary production, coincide with ocean outfall locations in central and southern California (Nezlin et al., 2012). Eutrophication can occur from excess nutrients entering the euphotic zone and cause algal blooms, dead zones, and hypoxia (Conley et al., 2009). Phytoplankton blooms in California coastal environments

have included several harmful algal species, such as dinoflagellates and diatom species in the *Pseudo-nitzschia* genus (Smith et al., 2018). These species threaten human health and cause marine mammal mass mortality (Anderson, 1997; Scholin et al., 2000).

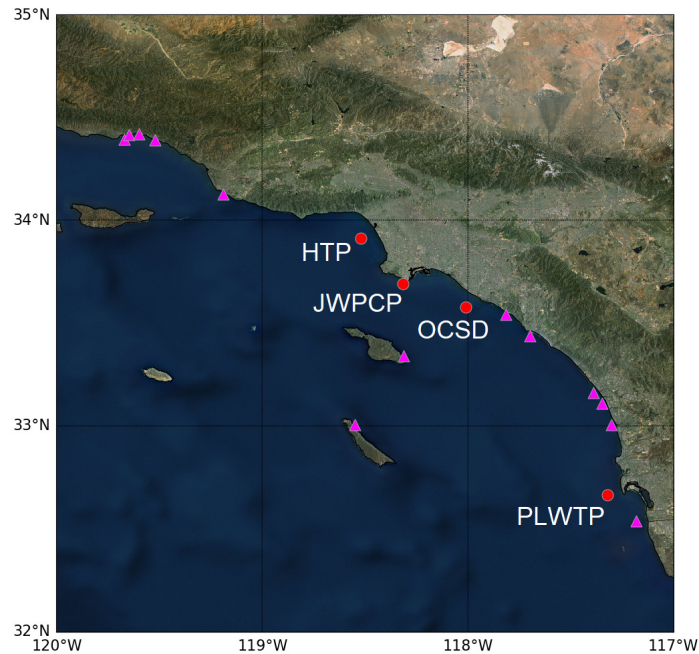


Figure 1.1: Location of all wastewater treatment plants that discharge into the Southern California Bight. Red dots indicate major dischargers and purple triangles indicate minor dischargers.

Effluent from the largest POTWs in the SCB is typically discharged at approximately 60 m depth and 8 kilometers offshore through diffusers. The pipes are bottom mounted and secured by ballast to protect against shoaling waves, current erosion, and seismic activity (Robertson, 2018). The diffuser is the end of the pipe that contains ports for effluent to exit and is usually about one kilometer long. Diffuser pipe diameter decreases from 4 to 1.8 meters seaward, which is designed to maintain the effluent flow velocity. Discharge ports are approximately 9 centimeters in diameter and have opposed or alternating port configurations on each side of the pipe. Opposed configuration has diffuser ports about every 7 meters while alternating has diffuser ports every 14 meters (Koh and Brooks, 1975). A photograph of a laboratory diffuser mimicking a wastewater pipe is shown in Figure 1.2. These diffusers are designed to encourage rapid mixing and sufficient offshore effluent dilution to restrict

plumes rise (Fischer et al., 1979; Wright et al., 1982). Preventing wastewater effluent from penetrating the surface is a priority for wastewater treatment plants; however, plumes have periodically reached the surface (Jones et al., 1990; Dalkey and Shisko, 1996; Gierach et al., 2017).

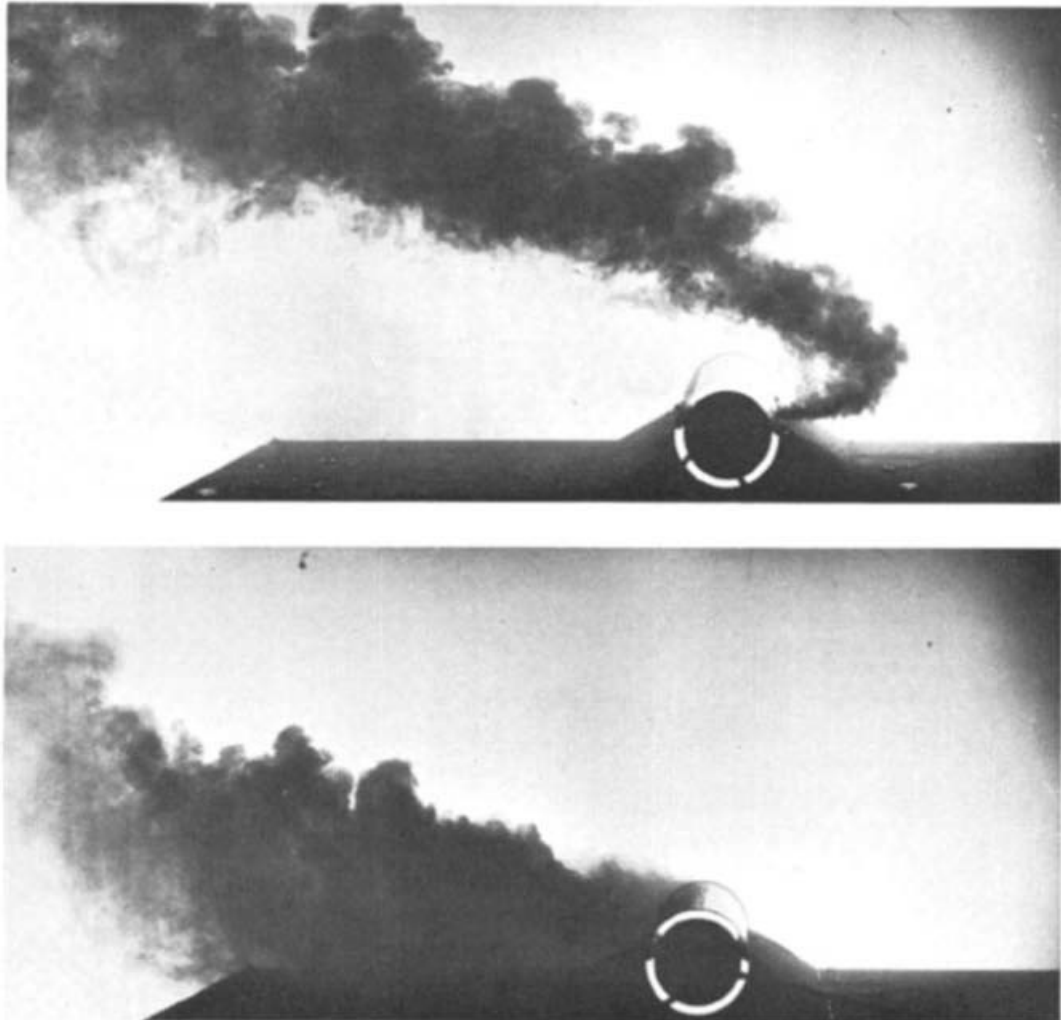


Figure 1.2: Laboratory simulation of a single port issuing a buoyant jet horizontally. Adapted from Koh and Brooks, 1975.

Wastewater treatment provides a critical freshwater source. Recently, southern California POTWs have begun reducing the total effluent volume discharged by extracting a portion of freshwater which decreases volume and increases discharge pollutant concentrations and density (OCSD, 2019; LACSD, 2019). A portion of secondary treated wastewater is treated

further through tertiary treatment and used to recharge groundwater (OCSD, 2019; LACSD, 2019). Initial mixing characteristics, far field plume establishment, and plume rise heights may be affected. Concomitantly resolving both near and far field mixing is identified as a fundamental challenge and future research area in wastewater plume modeling (Zhao et al., 2011).

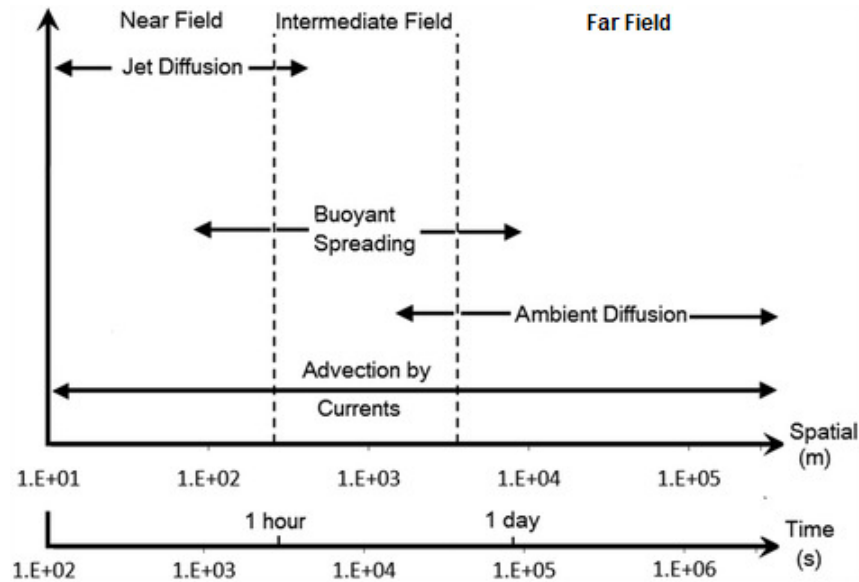


Figure 1.3: Physical processes of discharged submerged wastewater and corresponding length and time scales. Adapted from Niu et al., 2011; Jirka et al., 1975.

## 1.2 Near and Intermediate Field Modeling

Near field processes are typically resolved using analytical or empirical approaches, while far field relies upon numerical simulation. Near field mixing is defined as the immediate mixing upon release from the diffuser and its interaction with ambient ocean conditions. The collapse of the initial turbulence generated by buoyancy forces specifies the near field terminus (Carvalho et al., 2002). Figure 1.3 briefly summarizes the spatio-temporal scales of each stage of plume development.

Turbulence generated from buoyancy and momentum of effluent discharge is the dominant process in near field mixing and results in plume mixing, intrusion into the water surface,

and lateral dispersion. Time and length scales are on the order of minutes and meters, respectively. Near and intermediate field modeling has traditionally focused on analytical, empirical or a mixed modeling strategy referred to as jet integral methods.

The Environmental Protection Agency (EPA) has compiled and adopted many of these near field models for free use and distribution (Frick et al., 2003), and has allowed large-scale wastewater treatment plants to use them to meet National Pollutant Discharge Elimination System (NPDES) permit requirements for initial dilution (Roberts et al., 2011; Robertson, 2018). Typical NPDES permits require a 100:1 dilution of effluent before the effluent exits the zone of initial dilution (ZID), which is defined as horizontal distance away from pipe equal to the depth of the pipe. For typical SCB marine outfalls, the ZID is approximately a 60 meter radius (Robertson, 2018). The implications of using these models to meet federal discharge permit requirements merit a discussion of the governing processes and assumptions.

### **1.2.1 Analytical and Empirical Models**

Simple analytical and empirical near field models (e.g., Roberts et al., 1989a,b; Frick, 2004) are widely used to calculate initial dilution plume rise height. Analytical models are closed-form mathematical solutions derived from simplifications of the governing equations and multiple assumptions, such as absolute diffusion, flow, pipe geometry, and plume shape. They are readily available and computationally tractable on typical desktop computers. However, these solutions are applicable only to highly specialized flow cases, unable to reflect the complexity of the coastal ocean, and typically restricted to model validation efforts. For example, Riddle et al., 2001 compared plume spread in a random walk particle tracking (RWPT) model to an analytical model and found the predicted concentrations to be in good agreement with the model (Lewis et al., 1997). Okubo and Karweit, 1969 presents a method to calculate longitudinal transport and diffusion from velocity shear and constant eddy diffusivities. Israelsson et al., 2006 used the analytical solution in Okubo and Karweit, 1969 to test computational efficiency of different Lagrangian numerical methods.

Idealized plume and jet properties have been derived from dimensional analyses (Fis-

cher et al., 1979) and augmented with empirical laboratory experiments deducing relative relationships for jet and plume characteristics such as velocity, concentration, dilution as a function of initial parameters (i.e., buoyancy, concentration, flow rate). Fischer et al., 1979 presents an excellent summary of the governing plume parameters of mass flux, momentum flux, and buoyancy flux for pure jets, pure plumes, buoyant jets, single buoyant jets, merging buoyant jets, and buoyant line plumes. These relationships have been extended to model environmental plumes. Laboratory experiment results are used to deduce empirical relationships, usually in the form of coefficients, between the dimensionless groups to scale to realistic, full-sized operations (Fischer et al., 1979; Zhao et al., 2011). Ernst et al., 1996 used a characteristic length scale from Fischer et al., 1979 to model sedimentation from buoyant jets. Empirical formulas for the maximum height of buoyant plumes in stably stratified conditions were found in Morton et al., 1956. Terminal rise height, the elevation where vertical momentum flux disappears, and plume entrainment have been measured from experiments ranging from pure jets to pure plumes, particle-laden plumes, and different ambient stratifications to form dimensional analyses (Konstantinidou and Papanicolaou, 2003; Mirajkar et al., 2015; Mirajkar and Balasubramanian, 2017). Empirical relationships on interactions of cross flow, parallel flow, and port spacing on buoyant plumes have also been developed (Roberts et al., 1989a,b).

Roberts, Snyder, and Baumgartner developed the RSB model, an empirical length-scale derived model based on towed tank experiments and applied to ocean outfalls (Roberts et al., 1989a,b,c; Frick et al., 2003). The experimental studies were done on multi-port T-shaped diffusers in linearly density-stratified conditions using a line source. The parameters examined in these studies were current speed,  $u$ , and direction,  $\theta$ , port spacing,  $s$ , effluent density,  $\rho_0$ , and horizontal jet velocity from either side of a T-shaped diffuser,  $u_j$ . Discharge is characterized by the source flux per diffuser length,  $q$  [ $\text{m}^2/\text{s}$ ], momentum,  $m$  [ $\text{m}^3/\text{s}^2$ ], and buoyancy flux,  $b$  [ $\text{m}^3/\text{s}^3$ ]:

$$q = \frac{Q}{L} \tag{1.1}$$

$$m = u_j q \tag{1.2}$$

$$b = \frac{g(\rho_a - \rho_0)}{\rho_a} Q \quad (1.3)$$

where  $Q$  [m<sup>3</sup>/s] is the total discharge,  $L$  [m] is the diffuser length, and  $\rho_a$  [kg/m<sup>3</sup>] is the ambient density at port level. The most important parameter controlling multiport near field diffuser dynamics is given by the plume Froude number, also known as Robert's  $F$ ,

$$F = \frac{u^3}{b} \quad (1.4)$$

and relates the current speed to the buoyancy flux of the source. A length scale,  $l_b$  [m]

$$l_b = \frac{b^{1/3}}{N} \quad (1.5)$$

is used to relate buoyancy flux to buoyancy frequency, or Brunt-Väisälä frequency,  $N$  [1/s] (Wright et al., 1982),

$$N = \left( -\frac{g}{\rho_a} \frac{d\rho}{dz} \right)^{1/2} \quad (1.6)$$

$l_b$  can be used to nondimensionalize the horizontal and vertical scales of different domains. Additionally,  $l_m$  [m]

$$l_m = \frac{m}{b^{2/3}} \quad (1.7)$$

relates the momentum to buoyancy. The nondimensional ratios

$$\frac{l_m}{l_b} = \frac{mN}{b} \quad (1.8)$$

and

$$\frac{s}{l_b} \quad (1.9)$$

can be derived as diffuser parameters that denote the importance of source momentum flux and port spacing, respectively.

Multiple  $F$  and  $\theta$  values were used to determine the effect of current speed, relative buoyancy flux, and direction of the source on established wastefield properties. The properties observed were wastefield thickness,  $h_e$ , height to top of plume,  $z_e$ , minimum dilution or maximum concentration at the end of the initial mixing region,  $S_m$ , and minimum dilution level height,  $z_m$ . Minimum dilutions,  $S$ , sampled at various distances away from the pipe,  $x$ , are

also observed. Wastefield properties are illustrated in Figure 1.4. Empirical relationships can then be characterized as a dimensional analysis by four independent parameters:

$$\frac{S_m q N}{b^{2/3}}, \frac{z_e}{l_b}, \frac{h_e}{l_b}, \frac{z_m}{l_b} = f\left(\frac{l_m}{l_b}, \frac{s}{l_b}, F, \theta\right) \quad (1.10)$$

where the parameters detailed above are normalized to the buoyancy flux and  $l_b$ .

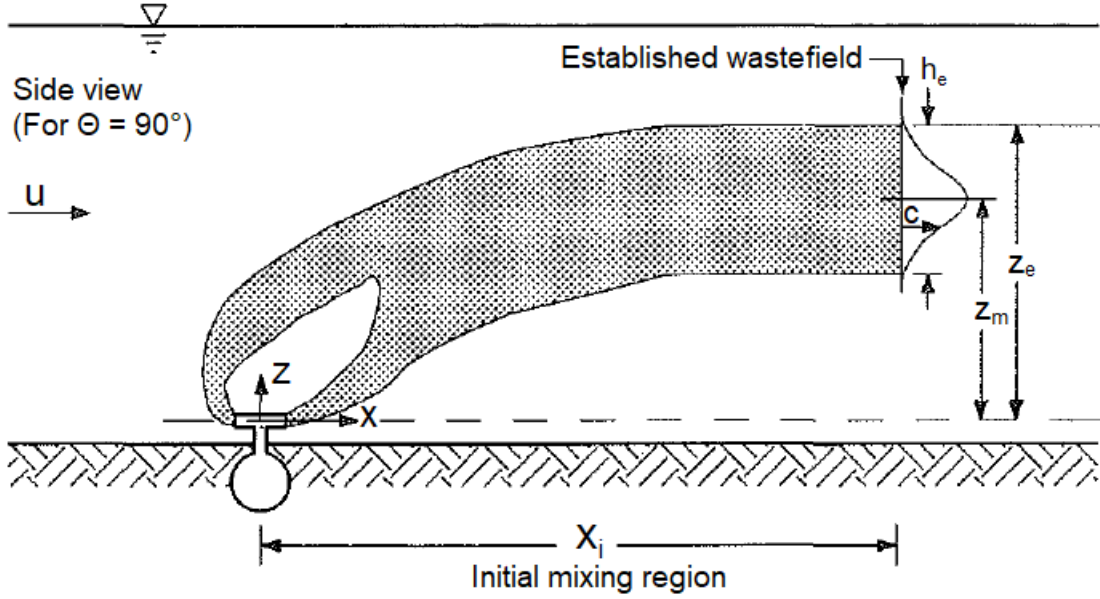


Figure 1.4: Diagram of observed characteristics of a multiport diffuser adapted from Roberts et al., 1989a.

### 1.2.2 Jet Integral Method

An alternative and popular approach is jet integral method which assumes a Gaussian jet profile based on the pioneering experimental work of Reichardt, 1941. Morton et al., 1956 established the jet entrainment hypothesis, which states that ambient nonturbulent fluid is entrained into the edge of the turbulent jet zone with a mean velocity proportional to mean centerline velocity (Morton et al., 1956; Jirka, 2004). The fundamental equations of conservation of momentum, mass, buoyancy, and concentration form the basis of the jet integral method. These jet integral models may be Lagrangian, where the independent variable is time, or Eulerian, where the independent variable is distance. Ordinary differential

equations are solved through integration along with the flow characteristics. The significant limitation of jet integral models is an assumption of an infinite receiving body of water that does not interact with boundaries (Bleninger and Jirka, 2004). Examples of the jet integrated method are CORMIX, VISJET, and Visual PLUMES.

### **1.2.2.1 CORMIX**

Cornell Mixing Zone Expert System (CORMIX) is a software system created in response to the EPA selected compilation of models that selects the appropriate hydrodynamic model from input data (Doneker and Jirka, 1991). The system uses dimensional analysis to classify the flow study into one of 35 categories and then selects a hydrodynamic model. The relevant submodel in CORMIX is CORJET, a Eulerian three-dimensional integral jet model for submerged single or multiple jets. CORJET can be used to predict plume characteristics such as initial mixing dilution, rise height of plume, and the mixing region (Doneker and Jirka, 2001; Carvalho et al., 2002). Kang et al., 1999 used CORMIX to predict near field dilution of wastewater discharge in Masan Bay in different seasonal conditions and compared the results to field measurements with limited success. Matos et al., 1998 similarly used near field CORMIX results with observed field studies and found difficulty in comparison because of lack of direct plume sampling.

### **1.2.2.2 VISJET**

VISJET is a software system used to visualize wastewater discharge based on the JETLAG model, a three-dimensional Lagrangian jet integral model. The visualization tool allows one to view a predicted plume in three-dimensions from different orientations (Lee and Chu, 2012). JETLAG (Lagrangian jet) is a generalization of the previous two-dimensional UM into three-dimensions and allows setting an initial jet discharge angle in respect to both vertical and horizontal discharge angles ( $\phi, \theta$ ). Unlike the UM3 model (discussed below), a varying entrainment coefficient is calculated from the local jet densimetric Froude number (jet momentum flux) and jet orientation ( $\phi, \theta$ ) (Lee and Cheung, 1990). Choi and Lee, 2007

developed a method to couple JETLAG model as a sub-grid plume model to fully resolve the near field into a three-dimensional far field model based on the Environmental Fluid Dynamics Code (EFDC).

### 1.2.2.3 Visual PLUMES

The EPA's Visual PLUMES is a software system with a selection of plume models that include the UM3 (Three-dimensional Updated Merge), DHKW (Davis, Kannberg, Hirst model for Windows), PDSW (Prych, Davis, Shirazi model for Windows), and RSB (NR-FIELD) models. The PDSW is a surface discharge model and as such, is not discussed here. Notably, Visual PLUMES is the preferred model system of OCSD.

The UM3 is a Lagrangian entrainment model based on the previous UM and UMERGE models (Frick, 1984; Frick et al., 1994; Frick, 2004). The assumptions made in the model are that the plume is steady state and is round in cross-section, a profile, such as Gaussian, describes velocity distribution and other plume properties, and flow in the wake of the plume next to the plume is tangent to the plume surface. The model solves the equations of conservation of mass, momentum, and energy at each time step. The continuity equation is

$$\frac{dm}{dt} = \rho_a b h (2\pi a |\underline{V} - \underline{U}| + \pi |\underline{U}| \cos \theta \frac{\partial b}{\partial s} + 2 |\underline{U}| \sin \theta + \frac{\pi}{2} b |\underline{U}| \sin \theta \frac{\partial \theta}{\partial s}) \quad (1.11)$$

where  $m$  is the mass of the element,  $t$  is time,  $\rho_a$  is the ambient density at the level of the element's center of mass,  $b$  is the radius,  $h$  is the plume height,  $a$  is the dimensionless shear,  $\underline{V}$  is the plume velocity vector,  $\underline{U}$  is the current vector,  $\theta$  is the angle the trajectory makes with the horizontal axis, and  $s$  is the distance measured along the trajectory. The momentum equation is

$$\frac{dm \underline{V}}{dt} = \underline{U} \frac{dm}{dt} - \frac{\rho_a - \rho}{\rho} g \quad (1.12)$$

where  $\rho$  is average plume density, and  $g$  is the acceleration of gravity. The energy equation is expressed in terms of enthalpy without considering conduction and radiation,

$$\frac{dm H}{dt} = H_a \frac{dm}{dt} \quad (1.13)$$

where  $H$  is plume enthalpy and  $H_a$  is ambient enthalpy. The model uses the Taylor en-

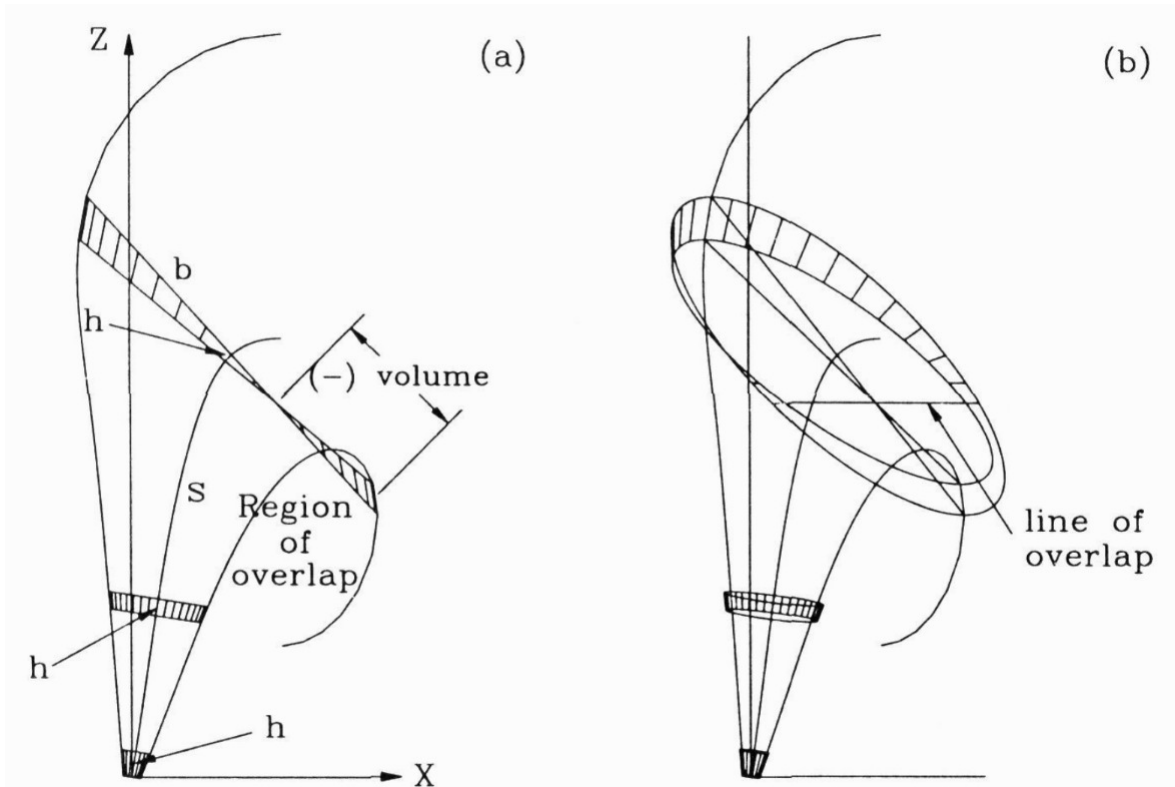


Figure 1.5: Lagrangian plume element at three stages of development indicated by black bars. (a) side view, and (b) oblique. Adapted from Frick et al., 1994.

trainment hypothesis, which relates the dilution rate to plume diameter and velocity shear between plume and stagnant ambient fluid (Morton et al., 1956), and projected area entrainment (PAE), which states that forced entrainment equals the product of current speed, ambient density, and area of the plume element projected onto the current (Frick, 1984; Frick et al., 1994). The inclusion of the Taylor entrainment hypothesis makes the model semi-empirical because the Taylor coefficients are derived from experiments. A constant Taylor coefficient is chosen in this model because of conflicting and ambiguous experimental results (Frick, 1984). Two-dimensional UM3 is illustrated in Figure 1.5. The model was modified to three-dimensions by adding a current component to the PAE hypothesis. UM3 assumes discharges from one side of the diffuser only where round buoyant jets can merge.

Also included in the Visual PLUMES software is the DKHW based on UDKHDEN (Frick et al., 2003). This model is a Eulerian three-dimensional model that can be used for single or

multiport diffusers. Assumptions include steady flow in the mean, hydrostatic assumption of pressure variations and incompressible fluid, ambient turbulence effects exist solely in the entrainment function, flow inside the jets is symmetric around the jet axis, and viscosity from the boundary layer affects this flow. Equations of motion for plume size, trajectory, concentration, and temperature are solved using the Eulerian integral methods (Frick et al., 2003). The governing equations are conservation of mass,

$$\frac{d}{ds} \int_0^\infty V r dr = E \quad (1.14)$$

conservation of energy,

$$\frac{d}{ds} \int_0^\infty V(T - T_\infty)r dr = \frac{dT_\infty}{ds} \int_0^\infty V r dr \quad (1.15)$$

conservation of pollutant,

$$\frac{d}{ds} \int_0^\infty V(C - C_\infty)r dr = -\frac{dC_\infty}{ds} \int_0^\infty V r dr \quad (1.16)$$

and conservation of momentum in the s equation,

$$\frac{d}{ds} \int_0^\infty V^2 r dr = UE \sin \theta_1 \cos \theta_2 + \int_0^\infty \frac{g(\rho_\infty - \rho)}{\rho_d} r dr \sin \theta_2 \quad (1.17)$$

where  $s$  is the distance along the plume's trajectory,  $V$  is the velocity,  $r$  is the radial distance,  $E$  is total volume energy density,  $C$  is the concentration,  $\rho$  is the average plume density,  $\infty$  indicates an element at some level,  $U$  is current speed,  $T$  is temperature,  $\theta_1$  is the horizontal angle between the plume centerline and the x-axis,  $\theta_2$  is the vertical angle between the plume centerline and the horizontal (Muellenhoff et al., 1985).

Carvalho et al., 2002 took field measurements of Ipanema beach outfall plume and used three near field models, RSB, UM3, and CORMIX, to predict dilution. Models reasonably predicted near field dilution with suitable assumptions but lacked the ability to capture the patchy nature of the wastefield.

Some studies have used three-dimensional models to derive dimensional analyses for the near field. Wang et al., 2011 examines the effect of buoyancy on buoyant jet penetration rate and the behavior of a starting buoyant jet in the period of flow development in a numerical

simulation at high-resolution grid scale. A Large-Eddy Simulation (LES) approach with Dynamic Mixed Model (DMM) is used, which utilizes a combination of Reynolds Average Navier-Stokes (RANS) and Direct Numerical Simulation (DNS) methods. The model uses the governing equations of spatially-filtered continuity, which separates eddies into grid scale and sub-grid scale components, RANS, and transport equations with Boussinesq approximation. A brief explanation of RANS, transport equations, and Boussinesq approximation is given in Sections 2.1 and 2.1.1. The focus of their study is the initial formation of buoyant jets and the penetration rate into quiescent environments. The resolutions of grid cells are orders of centimeters and domain of less than 2 meters whereby they attempt to resolve the first interactions of plumes with the ambient fluid in the near field. The numerical simulations are validated against the laboratory tank experiments of Wang and Law, 2002; Ai et al., 2005, 2006 and analytical expression in Hunt and Kaye, 2001. Non-dimensional relationships of total penetration distance are derived through numerical experiments as a linear combination of penetrative distances from initial buoyancy and initial momentum fluxes (Wang et al., 2011).

Although some near field models include far field modules (e.g., Doneker and Jirka, 2001; Frick, 2004), they are steady state and cannot account for spatio-temporal variability. Critically, near field models do not account for many physical phenomena inherent to ocean outfall discharge and plume evolution such as bottom topography, waves, tides, and rotation of the Earth.

At the end of the near field regime where jet momentum and turbulence dominate and before the wastefield is established, the intermediate field is at play (Zhao et al., 2011). The processes occurring in this near-far field transition depend on near field mixing and ambient flow that can affect ambient stratification, concentration, and gravity dispersion (Choi and Lee, 2007).

## 1.3 Far field Modeling

Far field mixing is defined as the drifting of the established wastefield and affected by ambient oceanic turbulence (Roberts, 1991). In the established wastefield, advection and diffusion determine plume dilution. Advection is a bulk transport process dominated by the mean current. In the context of outfall plumes, diffusion is the combined effects of molecular diffusion, turbulence, and shear instabilities (Kim et al., 2000). Typical time and length scales are on the order of hours and kilometers.

Far field 3-D numerical models (e.g., Blumberg and Mellor, 1987; Bouma et al., 2007) can determine plume characteristics and drifting away from pipe in an ocean environment but lack the grid size resolution to resolve near field mixing. Far field mixing has been modeled using a number of hydrodynamic models (e.g., MIKE, DELFT3D, EFDC, ROMS) using a Eulerian approach for flow resolution and Lagrangian for plume development (Kim et al., 2001; Blumberg et al., 1996; Uchiyama et al., 2014).

### 1.3.1 Lagrangian Plume Dispersion Modeling

A Lagrangian approach has been widely applied as tracer dispersion in buoyant plumes and jets (e.g., Kim et al., 2000, 2001, 2002; Israelsson et al., 2006). In contrast to directly solving the advection-diffusion equation, turbulent diffusion is simulated by the RWPT where the displacement of each particle is determined by an independent, random Markovian coefficient (Kim et al., 2002). Individual particles are individually tracked in space and time, and concentration is recovered from the number of particles in a given volume. Prototypical particle tracking equations are presented in Zhao et al., 2011. RWPT presents key challenges; concentration field depends on particle density per grid cell, becomes less accurate with long simulations and increasing distance from source, and computing costs limit large particle number simulations (Zhao et al., 2011). Additionally, diffusion coefficients must be chosen empirically (Kim et al., 2002). Lagrangian based RWPT methods are most applicable near point sources with high concentration gradients (Israelsson et al., 2006; Periez and Elliott, 2002).

### 1.3.2 Eulerian Modeling

Eulerian numerical models solve the advection-diffusion equation, or transport equation, for a given input of tracer (i.e., effluent). Directly solving this equation using finite difference, finite element methods, or finite volume method is more appropriate in far field modeling for long timescales and complex domains (Zhao et al., 2011). Implementation of these methods can lead to negative consequences such as numerical diffusion and dispersion, artificial oscillation, and inaccurate values in high gradient cases (Zhao et al., 2011). Wastewater constituents and properties are essentially highly diluted within the volume of the grid boxes of initialization (Zhang and Adams, 1999). Parameterization of tracer input into a fixed grid cell volume causes uniform mixing of the tracer concentration, which can lead to overestimation of mixing. A grid of appropriate resolution for the study area and accurate boundary conditions for the domain should be used (Zhao et al., 2011). Methods to create horizontal and vertical concentration profiles to mitigate this have been implemented (Uchiyama et al., 2014). Hydrostatic assumptions are common in ocean circulation and far field models and are discussed in Section 2.1.1. Hydrodynamic and oceanic models that have been used to model the far field include MIKE 21, DELFT3D, and ROMS (Pritchard et al., 2013; Morelissen et al., 2013; Uchiyama et al., 2014).

MIKE is a commercial modeling software that contains various two-dimensional (MIKE21) and three-dimensional (MIKE3) hydrodynamic models. MIKE 21 is a two-dimensional hydrostatic, Boussinesq, depth-averaged hydrodynamic model with cell-centered finite volume method to solve the two-dimensional Reynolds averaged Navier-Stokes equations (Pritchard et al., 2013). Nesting of high-resolution grids in lower ones are possible as well as a flexible mesh. The technique used to integrate the vertically integrated two-dimensional Navier-Stokes equations to the space-time domain is the Alternating Direction Implicit (ADI). MIKE 21 is useful for coastal applications because of the applicability to shallow and intermittently wet/dry systems that are well-mixed, and a plume can be implemented through the ECOLab toolbox in MIKE (Pritchard et al., 2013). However, 2D applications are limited because plume characteristics defined by height, such as height to top of the plume, are

unable to be resolved and consequently, limited to surface plumes and to impact assessment (e.g., Gourbesville and Thomassin, 2000; Tomicic et al., 2001). MIKE3 solves the hydrostatic momentum and continuity equations in three-dimensional Cartesian coordinates and is able to account for bathymetry, temperature and salinity conservation, tidal events, meteorology, currents, and other hydrographic conditions in its unsteady flow simulation (Moharir et al., 2014). This model can be used for the design and operation of wastewater diffusers, environmental impact assessment, sediment dynamics studies, sea ice simulations, and forecasting of water quality and ecological parameters. Rasmussen et al., 2000 used MIKE3 to model the transport of nutrients and eutrophication motivated by macroalgae bloom increase from wastewater discharge. MIKE3 has been coupled with near field model PROMISE to simulate the dispersion of wastewater in non-steady state environments and reported good agreement with laboratory measurements (Niu et al., 2011).

Delft3D is a modeling framework developed by WL|Delft Hydraulics with Delft University of Technology and contains many modules that allow modeling of hydrodynamic flow, transport of material, wave propagation, and other processes such as ecological and water quality. Delft3D-FLOW is a module within DELFT3D that has high applicability to coastal, estuarine, and river problems. Online (simultaneous) hydrodynamic computations of salinity and heat transport are used and the model can solve either the unsteady shallow-water equations in two- (depth-averaged) or three-dimensions. The governing hydrodynamic equations are horizontal momentum, continuity, transport, and  $k-\epsilon$  turbulence closure (Lesser et al., 2004). The model uses the hydrostatic assumption and Boussinesq approximations. Different grids can be chosen from Cartesian, orthogonal curvilinear, spherical, or for three-dimensions,  $\sigma$ -coordinate (topography-following, free surface). The Generalized Lagrangian Mean reference frame is used to solve the hydrodynamic equations in simulations with waves which allows more accurate expression of wave-induced driving forces (Lesser et al., 2004). Similar to MIKE 21, Delft3D-FLOW uses ADI to solve equations of momentum and continuity. The model uses the third-order upwind horizontal advection scheme split into four components for discretization called the “cyclic method”, a finite volume approximation. Horizontal diffusion is handled by an algorithm to approximate diffusion along z-planes in a  $\sigma$ -coordinate

mode and a horizontal Forester filter (Lesser et al., 2004). Delft-3D has been used nonhydrostatically to model coalescence of coastal river plumes (Warrick and Farnsworth, 2017). Morelissen et al., 2013 developed a dynamic, two-way coupling of CORMIX and Delft3D-FLOW in a hydrostatic environment and validated to thermal and freshwater wastewater discharge.

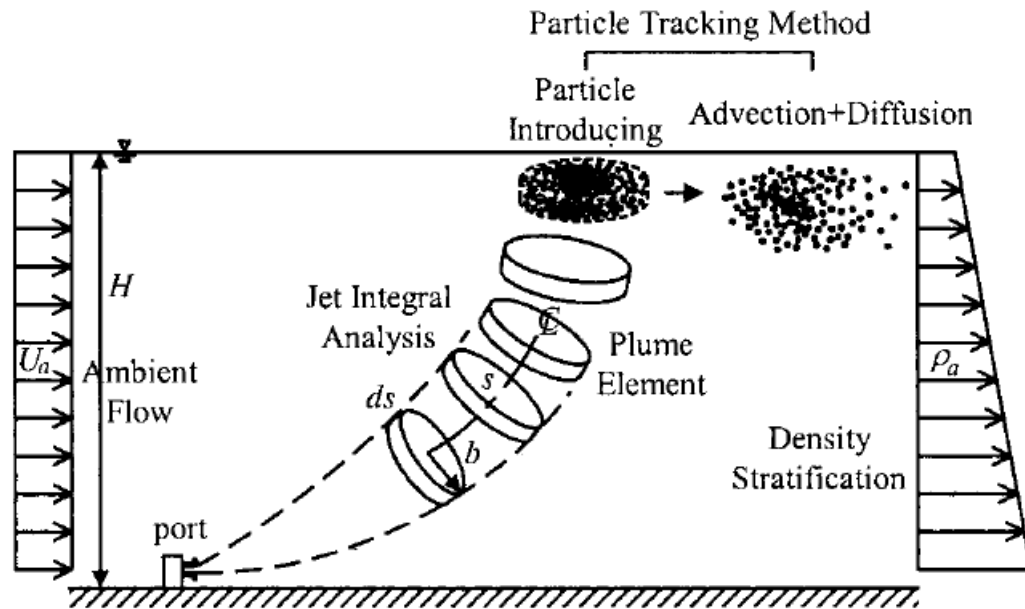


Figure 1.6: Conceptual diagram of using a near field jet integral model to initialize a Lagrangian RWPT model. Adapted from Kim et al., 2002.

Far field models have been coupled with near field models to more realistically resolve wastefield progression (Blumberg et al., 1996; Zhang and Adams, 1999; Roberts, 1999; Kim et al., 2001; Morelissen et al., 2013). However, the coupling is often one-way in which the near field models simply initialize location and concentration of the effluent for the far field model and/or the far field model computes the ambient conditions for the near field. For example, Zhang and Adams, 1999 proposed different methods to introduce source flow and pollutant loading into far field models from near field model results. A graphic of a method to couple a jet integral model with a RWPT model is shown in Figure 1.6. Choi and Lee, 2007 employs the Distributed Entrainment Sink Approach (DESA), a sub-grid plume model, to fully resolve the near field within a far field model. However, the near field model used for coupling must be similar to JETLAG, where entrainment flow can be calculated for plume

elements and as a sink of ambient water. Critically, model coupling is lacking (Choi and Lee, 2007). Furthermore, Botelho et al., 2016 remarks far field plume models have been prohibitive in resolving vertical acceleration terms in the nonhydrostatic RANS equations. A high-resolution, nonhydrostatic approach to facilitate tightly coupled intermediate and far field dynamics with parameterized near field processes has not been examined in the literature.

Historically, wastewater plume modeling has been difficult to resolve because of separate near field and far field mixing models. The objective of this research is to develop and validate a tightly coupled hydrodynamic model capable of resolving both intermediate and far field mixing. An unprecedented high-resolution ( $\sim 1\text{m}$ ) nonhydrostatic ROMS model is developed, tested and validated against Roberts et al., 1989a,b,c experiments. Model development is presented in Chapter 2. Results are described in Chapter 3, discussed in Chapter 4 and followed by conclusions and future work in Chapter 5.

## CHAPTER 2

### Modeling Approach

#### 2.1 High-Resolution Nonhydrostatic ROMS Model

The Regional Ocean Modeling System (ROMS) is a terrain-following-coordinate, split-explicit time-stepping oceanic model that solves the hydrostatic, free-surface primitive equations in a rotating environment and uses a K-profile parameterization (KPP) for turbulence closure (Large et al., 1994) with Boussinesq approximations (Shchepetkin and McWilliams, 2003, 2005). The modeling system uses the Arakawa C-grid (Arakawa and Lamb, 1977) for model state variables (Haidvogel et al., 2008). ROMS has many applications and a majority of simulations are large-scale  $O(10 - 100 \text{ km})$  (Marchesiello et al., 2003; Penven et al., 2005). Recent ROMS simulations have moved from mesoscale to submesoscale (Gula et al., 2015; Molemaker et al., 2015; Dauhajre et al., 2017) and focused on local and coastal regions (Howard et al., 2014; Uchiyama et al., 2014). ROMS solves the three-dimensional momentum (RANS), continuity, and tracer equations. Separate barotropic and baroclinic modes are calculated using the split-explicit time stepping method (Shchepetkin and McWilliams, 2003, 2005). The Navier-Stokes equations in Cartesian coordinates ( $x$ -axis eastward,  $y$  northward,  $z$  upward) with Earth's rotation are

$$\frac{Du}{Dt} - 2\Omega_z v + 2\Omega_y w = -\frac{1}{\rho} \frac{\partial P}{\partial x} + F_u, \quad (2.1)$$

$$\frac{Dv}{Dt} + 2\Omega_z u - 2\Omega_x w = -\frac{1}{\rho} \frac{\partial P}{\partial y} + F_v \quad (2.2)$$

$$\frac{Dw}{Dt} + 2\Omega_x v - 2\Omega_y u = -\frac{1}{\rho} \left( \frac{\partial P}{\partial z} + g\rho \right) + F_w \quad (2.3)$$

where  $\frac{D}{Dt} = \frac{\partial}{\partial t} + \mathbf{u} \cdot \nabla$  represents a Lagrangian derivative or advective time derivative,  $\mathbf{u} = (u, v, w)$  is flow field velocity vector,  $\boldsymbol{\Omega} = (\Omega_x, \Omega_y, \Omega_z)$  is the angular velocity of rotation

of the Earth,  $\rho$  is density of seawater,  $P$  is pressure, and  $F$  is forcing and dissipation terms for the respective variables. Conservation equations of advection-diffusion for heat content and tracers are

$$\frac{D\Theta}{Dt} = F_{\Theta}, \quad \frac{DS}{Dt} = F_S \quad (2.4)$$

where  $\Theta$  is potential temperature, and  $S$  is salinity. To discretize advection, ROMS utilizes the third-order upstream, or upwind, biased advection scheme by a UTOPIA-like algorithm (Uniformly Third-Order Polynomial Interpolation Algorithm) (Shchepetkin and McWilliams, 1998, 2005). Horizontal tracer advection is constructed through this finite volume method (Haidvogel et al., 2008). This scheme accounts for eddy diffusivity by a numerical hyperdiffusion related with the horizontal advection with an effective diffusivity coefficient that decreases with the grid scale (Uchiyama et al., 2014). Vertical tracer advection is handled by a conservative parabolic spline (Haidvogel et al., 2008). The Equation of State (EOS) is given by

$$\rho = \rho(\Theta, S, P) \quad (2.5)$$

and closes the above system of equations by coupling heat and salinity (Kanarska et al., 2007).

The topography-following coordinate system has a full three-dimensional transformation of

$$z = Z(x, y, \sigma, t), \quad -1 \leq \sigma \leq 0 \quad (2.6)$$

where  $z$  is the Cartesian height,  $\sigma$  is the vertical distance from the surface of the water column as a fraction of the column thickness, and  $Z$  is a monotonic (i.e.,  $\partial Z/\partial \sigma > 0$ ) and nonseparable (i.e., nonlinear stretching  $S(\sigma)$  is not independent of horizontal coordinates) mapping function (Shchepetkin and McWilliams, 2003, 2005).  $\sigma = 0$  is the free surface and  $\sigma = -1$  is the oceanic bottom. The continuity equation is

$$\frac{\partial \rho}{\partial t} + \nabla \cdot (\rho \mathbf{u}) = 0 \quad (2.7)$$

### 2.1.1 Hydrostatic versus Nonhydrostatic

The hydrostatic approximation simplifies many of the equations listed above. For the continuity equation, incompressible fluid is assumed, and mass continuity becomes a volume continuity equation:

$$\nabla \cdot \mathbf{u} = 0 \quad (2.8)$$

This is also known as the nondivergence equation. Equation 2.3 for vertical momentum is replaced with the vertical force balance

$$\frac{\partial P}{\partial z} = -\rho g \quad (2.9)$$

where vertical pressure gradient balances buoyancy force, and vertical velocity,  $w$ , is computed from Equation 2.8 (Kanarska et al., 2007). Vertical accelerations are assumed to be small compared to gravitational acceleration,  $g$ . This relationship is derived because the vertical velocity  $w$  is assumed to be small. To illustrate this, an aspect ratio from ocean length scales  $L$  and  $H$ , representing horizontal and vertical length scales respectively, can be determined. In typical ocean domains with large-scale flow, the aspect ratio ( $H/L$ ) is often very small. For example, in ocean gyre circulation, the horizontal scale  $L$  is usually 1000 kilometers and the depth scale,  $H$ , is 1 kilometer (Williams and Follows, 2011). The magnitude of  $w$  can be approximated as  $w \sim u(H/L)$ . Therefore, the small aspect ratio implies  $w$  is much smaller than  $u$ . As a result, the terms on the left-hand side of Equation 2.3 are much smaller than  $g$  (Williams and Follows, 2011). The vertical momentum is dominated by the horizontal momentum terms, and vertical velocity can be calculated from the nondivergence equation using horizontal velocities (McWilliams, 2006).

Compressibility is not negligible in its effect on  $\rho$  in deep water, and the EOS must be corrected. Pressure in Equation 2.5 is modified to use  $P_0(z)$  instead of dynamic pressure. Incompressibility also causes acoustic waves to be neglected because they move by density variations. The Boussinesq approximation omits density variations in the momentum equations except when contributing to the buoyancy force. In other words,  $\rho$  is replaced with a reference density  $\rho_0$  except when multiplied by  $g$  and in the EOS (McWilliams, 2006; Williams and Follows, 2011). Another hydrostatic simplification involves the Coriolis force

where terms proportional to  $\Omega_x$  and  $\Omega_y$  are neglected, also known as the “traditional approximation”, causing an incomplete angular-momentum principle and underestimating the Coriolis force (Kanarska et al., 2007).

The move from hydrostatic to nonhydrostatic is desirable for resolving small scale phenomena requiring a prognostic vertical momentum equation and small grid resolutions, such as buoyant plumes. The aspect ratio  $H/L$  is close to one for plumes because horizontal and vertical velocity magnitudes are similar based on preliminary tests with no ambient flow. Vertical velocities become important in the plume regime. The hydrostatic assumption is removed and the above constraints are relaxed except for incompressibility and the Boussinesq approximation (Guillaume et al., 2017). The main change from a hydrostatic model to nonhydrostatic dynamics is the use of Equation 2.3 to calculate vertical momentum instead of Equation 2.9. As simulations increase in resolution and horizontal length scales decrease, the hydrostatic assumption of vertical momentum becomes less accurate and vertical momentum must be solved from the RANS equation. Plume characteristics can be more accurately resolved for vertical mixing and plume rise. Convection is an important process in the development of buoyant plumes that is better resolved with nonhydrostatic dynamics (Morton et al., 1956; Guillaume et al., 2017). Preliminary results show differences in plume height rise and dilution between hydrostatic and nonhydrostatic simulations and are outlined in Figure 2.1. In ROMS, the KPP turbulence closure scheme is removed in the nonhydrostatic simulations.

Critically, near field mixing violates the hydrostatic assumption that pressure is simply a function of density, gravity, and depth and ignores vertical acceleration by replacing the vertical momentum equation with the hydrostatic approximation. Buoyant plume modeling using the hydrostatic assumption cannot adequately resolve mass transport and are limited in predicting fate and transport at small scales (Nekouee et al., 2015). Different dispersion mechanisms for near field and far field processes require an improved coupling of the techniques and intermediate field simulations (Zhao et al., 2011).

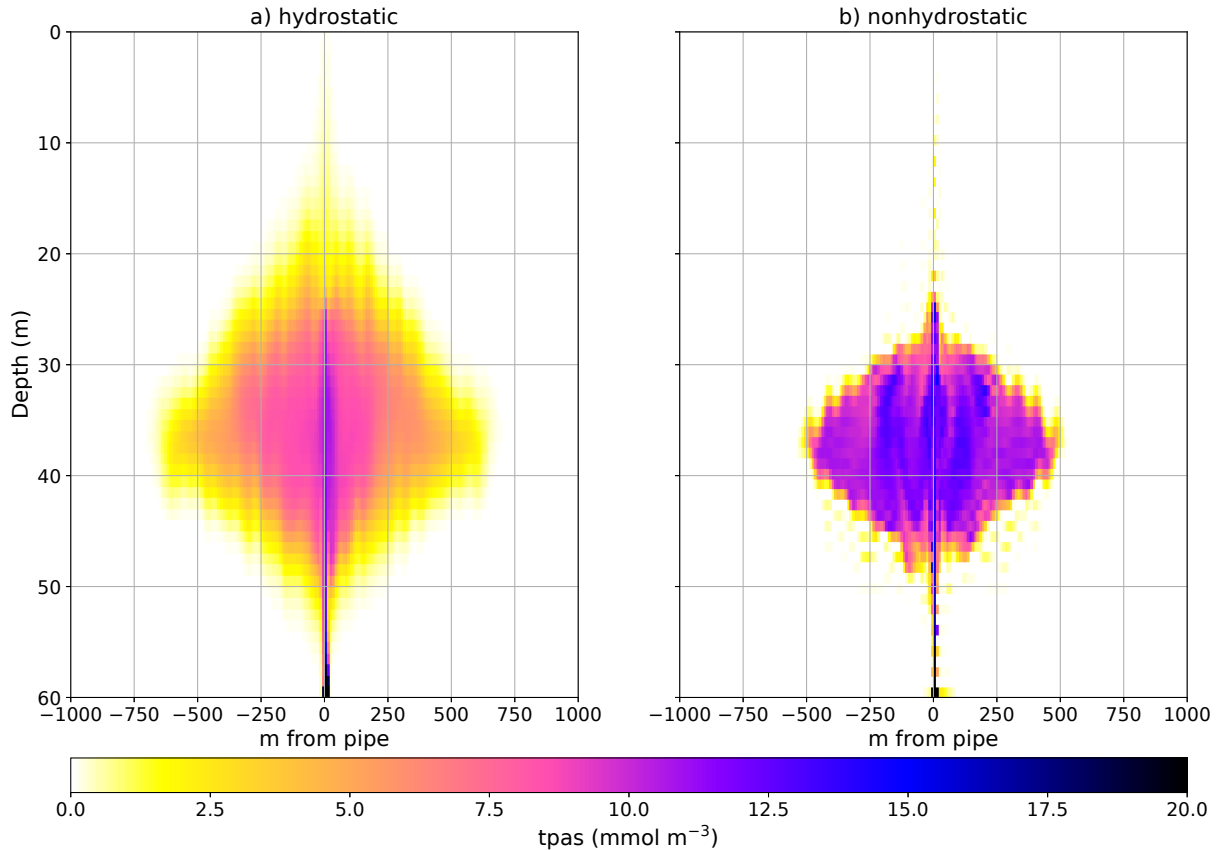


Figure 2.1: Instantaneous fields of ROMS zero current plume simulations at 10 meter horizontal resolution with hydrostatic approximation on (a), and off (b). The plume is excessively buoyant and overly diffused in the hydrostatic simulation. Plume is represented by a passive tracer, *tpas*. KPP turbulence closure is present in the hydrostatic model and not present in the nonhydrostatic.

## 2.2 Validation Data

The laboratory experiments of Roberts, Snyder, and Baumgartner (RSB) are chosen for comparison to the Regional Oceanic Modeling System for two primary reasons: i) multiple far field models have used the RSB model to initialize the established wastefield, including ROMS (Zhang and Adams, 1999; Kim et al., 2001; Uchiyama et al., 2014), and ii) the EPA has adopted the RSB model (based on the RSB experiments) to meet wastewater treatment NPDES dilution permits (Roberts et al., 2011; Robertson, 2018). Additionally, OCS&D used the model in 2002 and 2008 in preparation of lowering their effluent discharge

and implementing their Groundwater Replenishment System (GWRS) (Robertson, 2018).

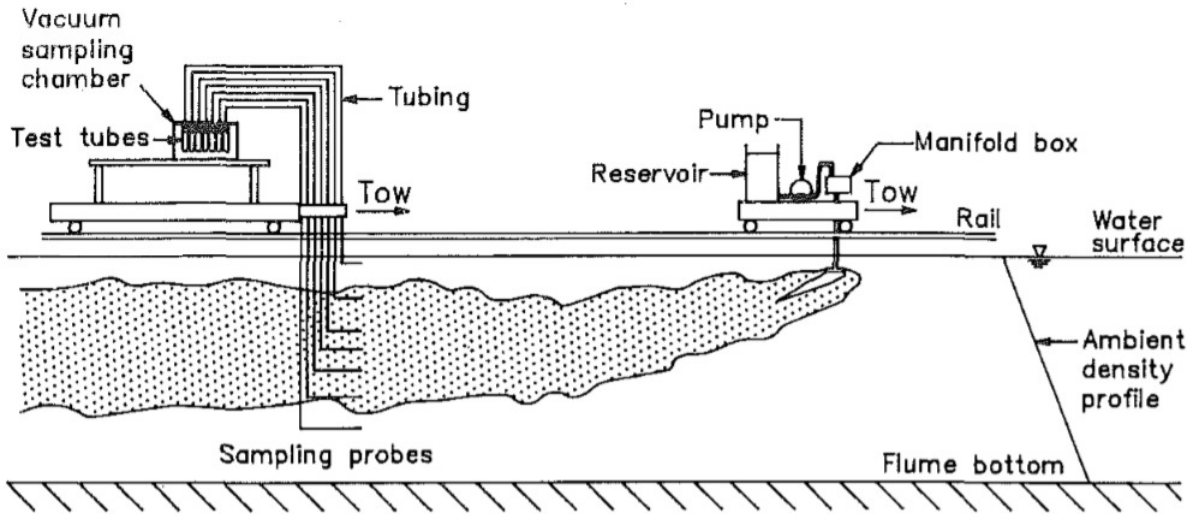


Figure 2.2: Schematic of RSB experimental configuration adapted from Roberts et al., 1989a. Tow tank was 25 meters long, 1.2 meters deep, and 2.4 meters wide.

RSB series 3 and 4 experiments are chosen as validation data for ROMS. These series correspond to perpendicular (cross) flow experiments on 25 T-shaped diffuser ports at Froude numbers 0, 0.1, 1, 10, and 100. The diffuser ports are moved along the length of the tank at speeds corresponding to the appropriate Froude number to mimic cross flow. Schematic of RSB laboratory structure is shown in Figure 2.2 and more detailed descriptions of experimental setup are in Roberts et al., 1989a. The specific parameters in these experiments have  $l_m/l_b \leq 0.2$ , the lowest momentum fluxes, and port spacing  $s = 5$  centimeters. These experiments are categorized as the line plume situation. This situation is one in which port spacing and jet momentum flux are negligible, and plume development is generated by buoyancy flux.

## 2.3 ROMS Plume Modeling

### 2.3.1 Model Grid

We run ROMS in a domain that is realistic in its length and height scales to ocean domains but with parameters that are used in the laboratory experiments. An idealized 1024 by 512

by 64 grid (3072 by 1536 by 60 m) with 3 meter horizontal and less than 1 meter vertical resolution with flat bottom bathymetry is used to model nearly all experiments. Experiments are also conducted with 1 meter and 10 meter horizontal resolution with the same vertical resolution, and results are presented in Section 3.2. Open boundary conditions are chosen with a zero gradient eastern boundary ( $du/dx = 0$ ) and 100 meter wide sponge layers on all boundaries to prevent boundary interactions with the outflow boundary. The magnitude of the sponge layer is  $0.1 \text{ m}^2 \text{ s}^{-1}$ . Friction at the oceanic bottom is turned off to allow a uniform current from the ocean surface to bottom. A wastewater pipe was implemented at the bottom of the vertical domain to mimic a bottom-mounted pipe typical to southern California marine outfalls (Section 2.3.2). The Coriolis force is set to zero to prevent the effects of the rotation of the Earth on the established plume.

### 2.3.2 Diffuser Representation and Effluent Flux Forcing

Effluent source forcing is parameterized as each grid cell has a volume of  $8.4375 \text{ m}^3$ . The incoming temperature, salinity, and passive tracer concentration are subject to grid size parameterization and become uniformly mixed within the grid cells that have effluent input. The turbulent mixing that occurs when the effluent first exits the pipe, therefore, is not resolved here. Roberts et al., 1989a notes that source momentum flux and port spacing do not significantly affect normalized dilution across all experiments and parameters tested. The individual plumes from each port merge to approximate a line source. Increased momentum flux causes decreased plume rise height though dilution is nearly constant.

Effluent tracer source forcing is shaped by diffuser geometry and dependent on resolution. Details of implementation are presented in Uchiyama et al., 2014. Relevant equations are the nondimensional tracer concentration equation with equivalent source  $P$  [1/s]

$$\frac{\partial c}{\partial t} = -\nabla \cdot \mathbf{F} + P \quad (2.10)$$

with

$$P(x, y, z, t) = P_s(t)A(x, y)H(z) \quad (2.11)$$

where  $c$  is pollutant concentration normalized by input pollutant concentration  $C_p$ .  $\mathbf{F} =$

$\mathbf{uc} + \mathbf{F}_{sgs}$  is the advection-mixing flux associated with resolved flow and sub-grid scale (*sgs*) parameterizations. The  $F_{sgs}$  here is the upwind advection scheme mentioned in Section 2.1. Pollutant species can be represented by multiplying  $c$  fields by inflow concentration  $C_p$ .  $A, H$  are the spatial functions mimicking unresolved near field mixing above the diffusers and have integrals equal to the source area and depth

$$\int \int A \, dx \, dy = A_s \quad (2.12)$$

and

$$\int H \, dz = H_s \quad (2.13)$$

where  $A_s$  is the horizontal area of the diffuser,  $H_s$  is the vertical size, and  $V_s = A_s H_s$  is the volume.  $P_s = Q_p/V_s$ , where  $Q_p$  is volume flux [ $\text{m}^3/\text{s}$ ].  $A, H = 1$  in the horizontal and vertical grid cells of the diffuser pipe that tile the bottom of the domain to uniformly force effluent volume flux over pipe area. No shape function is fitted to  $H$  in order to mimic bottom mounted pipes.  $A_s = N_s dx^2$  and  $N_s$  is the number of cells that make up the diffuser.  $N_s = 3000$  for  $dx = 3$  m,  $N_s = 15000$  for  $dx = 1$  m, and  $N_s = 270$  for  $dx = 10$  m. Length and width of the pipe are given below.

The RSB experiments are presented nondimensionally and can be translated into realistic applications. Pipe geometry, effluent properties, and ambient ocean conditions were obtained from OCSD and used to model the RSB tank experiments in a domain typical to wastewater treatment plants in the southern California Bight. However, a linearly stratified vertical profile was implemented to match conditions in the tank experiments.

A constant effluent volume flux of  $Q_p = 10 \text{ m}^3 \text{ s}^{-1}$  is forced uniformly over a pipe of width 30 meters and length 900 meters in the 3 meter resolution experiments. A random input of volume flux on the order of  $10^{-6} \text{ m}^3 \text{ s}^{-1}$  is applied to each effluent input grid cell in  $N_s$  to induce randomness and facilitate startup of experiments. The resolution and present configuration of the ROMS experiments are unable to represent the sideways momentum of the diffuser ports. The 900 meter length pipe is chosen to represent the bottom of the “L”-shaped portion of the OCSD 5-mile pipe that is aligned along the 60 meter bathymetry contour (see Figure 2.3, red circle). Preliminary testing of pipe source width was done, and

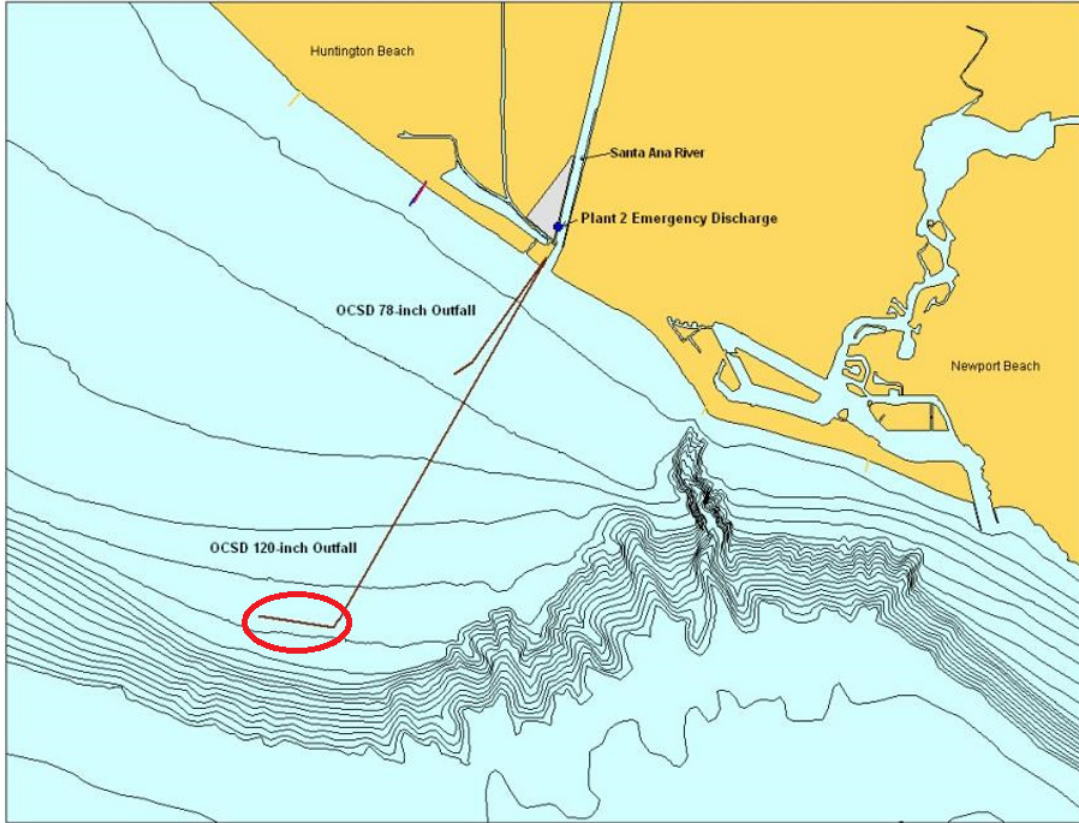


Figure 2.3: Representation of OCSD pipes. Black lines are bathymetry contours and brown lines are OCSD pipe. The pipe in regular use is the 120-inch outfall and is often called the “5-mile pipe”. The shorter 78-inch outfall is used only in emergency situations and during diversions for maintenance on the 5-mile pipe. Red circle is idealized pipe modeled in this study. Adapted from Rogowski et al., 2014.

30 meters is chosen to uniformly mix incoming effluent to mimic initial dilution. The volume flux per grid cell is dependent on the size of the diffuser and resolution of grid cells. For 3 meter resolution experiments, the volume flux per grid cell is  $0.00333 \text{ m}^3 \text{ s}^{-1}$ . The 1 meter experiment is  $0.00037 \text{ m}^3 \text{ s}^{-1}$ ; the 10 meter is  $0.03704 \text{ m}^3 \text{ s}^{-1}$ ; the smaller pipe width is  $0.00666 \text{ m}^3 \text{ s}^{-1}$ . The configurations of the various ROMS experiments are detailed in Table 2.1.

The pipe is placed in the middle of the domain in the x-direction for  $F = 0$  to allow western and eastern plume spread. The pipe is placed a quarter into the domain in the

x-direction for  $F \geq 0.1$  to allow more distance to be observed downstream of the pipe.

### 2.3.3 High-Resolution Nonhydrostatic ROMS Validation Experiments

Validation is conducted by nondimensionalizing the ROMS parameters of cross flow velocity,  $u$ , buoyancy frequency,  $N$ , and buoyancy flux,  $b$ , into the Froude number relationship  $F$  (Equation 1.4) and length scale  $l_b$  (Equation 1.5). Source flux calculated from Equation 1.1 is  $q = Q_p/L = 1/90$ . Typical effluent temperature, salinity, and ammonium are chosen as 26.9°C, 1.2 PSU, and 1500 mmol m<sup>-3</sup>. Ammonium is represented here by a nonreactive passive tracer ( $C_p$ ), which is used to measure dilution.

The flow speed for each experiment was calculated by selecting Froude numbers 0.1, 1, 10, and 100 and solving  $u = (Fb)^{1/3}$ . The corresponding velocities in m s<sup>-1</sup> are 0.0668, 0.14395, 0.31013, and 0.66817, respectively, assuming the buoyancy is calculated from Equation 1.3 with  $\rho_a = 1025.5403$ .  $F = 10$  and 100 flows are atypical in the SCB where 0.3 m s<sup>-1</sup> is near the highest end of the spectrum of flow velocities. Typical flow velocities in the region are between 0.05 and 0.25 m s<sup>-1</sup>, or  $\sim F = 0.1$  and 1.

ROMS experiments were run on computer Maya in UCLA Center for Earth Systems Research laboratory on 128 to 256 cores with MPI parallelization. Each experiment was run for 11.75 hours to give sufficient time for the region of interest to reach steady state. Time stepping value is cross flow velocity and resolution dependent with higher velocities and resolutions requiring lower time step to meet the Courant-Fredichs-Lewis (CFL) condition (Courant et al., 1967). Time steps ranged between 0.3 and 7.5 seconds. Total wall clock time for experiments was between 2 to 96 hours. Output was saved every 15 minutes.

Results are normalized through the dimensional analyses presented in Roberts et al., 1989a,b.  $F = 0$  and 0.1 model runs are averaged over the last 1.25 hour of the experiment while  $F = 1, 10$ , and 100 are averaged over the last 3.5 hours for all analyses. These experiments are averaged over time to ensure incidental perturbations are smoothed out. Less time is averaged for lower Froude numbers because the wastefield requires more time to be established and reach the eastern boundary. Model validation results are also averaged

over the length of the pipe because all are cross flow experiments.

#### 2.3.4 Ambient Stratification

A linearly density-stratified vertical profile is uniformly implemented in the horizontal domain with winter conditions that are similar to the ambient conditions near the pipe of Orange County Sanitation District (see Figure 2.4). This vertical profile is created by taking the average of all available wintertime CTD (conductivity, temperature, depth) observational data within a 3 by 3 km area around the OCSD pipe and creating a linear profile between the surface and ocean bottom values (Robertson, 2018). The RSB experiments discharged negatively buoyant effluent into linearly density-stratified water created by filling their tank with saltwater. All RSB experiments used a buoyancy flux between  $9.8 \times 10^{-5} - 1.1 \times 10^{-4} \text{ m}^3 \text{ s}^{-3}$  and buoyancy frequency of  $0.3 \text{ s}^{-1}$ . The linearly stratified density profile in ROMS is forced through both temperature and salinity profiles, and the buoyancy frequency is  $0.010997 \text{ s}^{-1}$  for all experiments. ROMS buoyancy flux is  $0.00298 \text{ m}^3 \text{ s}^{-3}$ .  $l_b$  is calculated from Equation 1.5 as 13.09012 m.

Experiment	Froude Number	Horizontal			Effluent	
		Cross-flow Velocity (m s <sup>-1</sup> )	Grid Resolution (m)	Effluent Temperature (°C)	Effluent Salinity (PSU)	Effluent Volume Flux per Grid Cell (m <sup>3</sup> s <sup>-1</sup> )
F0	0	0	3	26.9	1.2	0.00333
F01	0.1	0.0668	3	26.9	1.2	0.00333
F1	1	0.14395	3	26.9	1.2	0.00333
F10	10	0.31013	3	26.9	1.2	0.00333
F100	100	0.66817	3	26.9	1.2	0.00333
F100 1 m	100	0.66817	1	26.9	1.2	0.00037
F100 10 m	100	0.66817	10	26.9	1.2	0.03704
F100 small pipe	100	0.66817	3	26.9	1.2	0.00666

Table 2.1: ROMS experimental parameters. For all experiments, buoyancy frequency  $N = 0.010997 \text{ s}^{-1}$  and buoyancy flux  $b = 0.00298 \text{ m}^3 \text{ s}^{-3}$ .

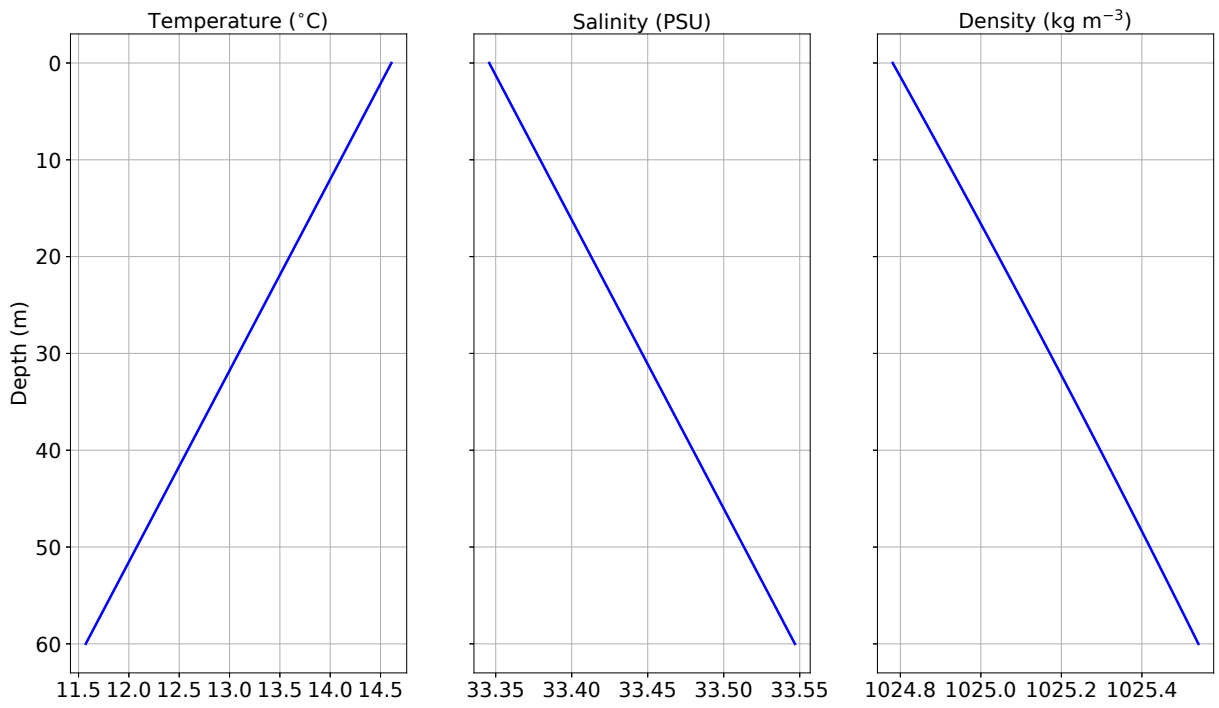


Figure 2.4: ROMS vertical temperature, salinity, and resultant density profile implemented across the horizontal domain of the simulations.

## CHAPTER 3

### Results

#### 3.1 ROMS RSB Validation Experiments

Domain centered along-pipe established wastefields with various Froude numbers and concentration gradients are shown in Figure 3.1. The  $F = 0$  simulation has the pipe in the middle of the domain and thus has less downstream distance from the pipe as the other experiments. The  $F = 0$  plume spreads up and downstream, but the upstream is not depicted here. At  $F = 0.1$ , no lateral spreading upstream occurs and all effluent is moved downstream. An overshoot of the plume equilibrium heights is observed for  $F \leq 1$  before they move to the neutral buoyancy height. Increasing the flow to  $F = 1$  shows the plume exhibiting oscillatory behavior (Figure 3.1(c)) that is discussed later in this section. Thickness and plume rise height decreases for increasing  $F$ .

Roberts et al., 1989a noted two different flow regimes for buoyant plumes, forced entrainment and free plume. The forced entrainment flow regime (e.g., Figure 3.1(d)) is observed when current speed is high and the bottom of the wastefield stays at the diffuser nozzle level. The buoyant plume flow pattern of entraining all the oncoming flow cannot be maintained and there is efficient mixing near the source (Cederwall, 1971). The free plume pattern (e.g., Figure 3.1(b)) occurs during low current speed and has normal plume-like characteristics with the plume curved downstream and entrainment of the ambient flow. Clear forced entrainment is observed in simulations  $F = 10$  and  $100$ , and free plume is observed in  $F = 0$  and  $0.1$ . Roberts et al., 1989a observed their  $F = 1$  experiment with features of both the forced entrainment and free plume regime. The  $F = 1$  model run accurately exhibits both forced ( $<750$  m) and free ( $>750$  m) characteristics (Figure 3.1(c)).

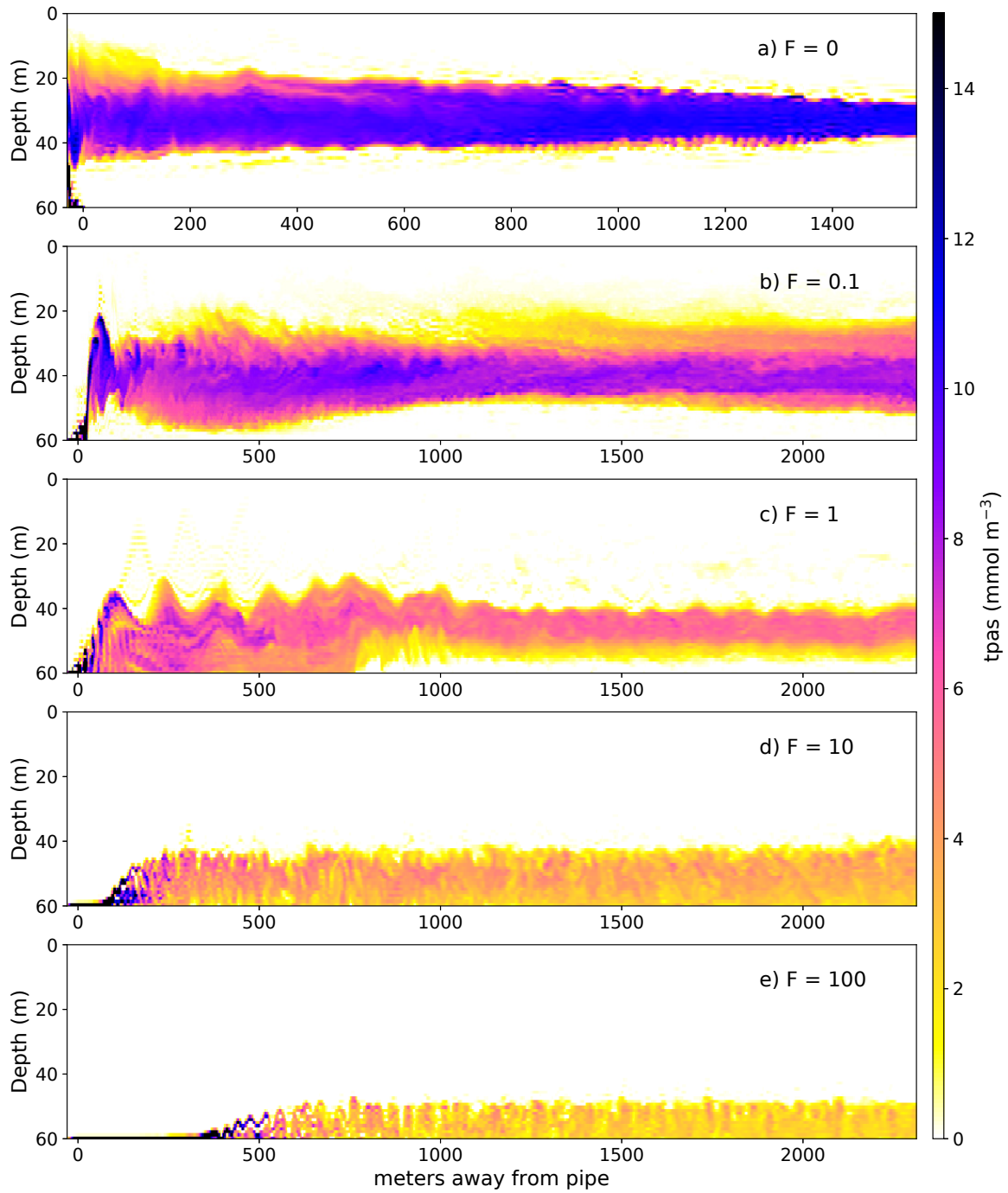


Figure 3.1: Instantaneous concentration fields of ROMS experiments  $F = 0, 0.1, 1, 10, 100$  after 11.5 hours from the center of pipe to the eastern boundary. Note only the right side of the domain of  $F = 0$  plume is shown with a smaller domain.

Plume dilution increases as current speed increases. In  $F = 0$ , continuous entrainment of effluent discharge above the pipe causes lateral spreading of the plume, and some mixing occurs, but the core of the plume is relatively uniform in concentration.  $F = 0.1$  and 1 show lower concentrations from the forcing of the ambient flow. Filaments of higher concentrations can be seen moving through the plumes. The forced entrainment flow regime in  $F > 1$  show incidental holes with little to no effluent concentration. As Froude number increases, some distance is required before the plume is able to lift off the bottom of the domain, which is not observed in the RSB experiments. This distance is most noticeable in 3.1(e) where effluent is carried approximately 300 m downstream in the bottom cell before observable entrainment occurs. Consequently, the minimum dilutions over distance are trapped at the bottom of the domain, and distance for the plume to rise and develop is considerably overestimated. The plume is expected to rise off the bottom cell closer to the diffuser.

Experiment	Froude Number	Minimum dilution ( $S_m q N / b^{2/3}$ )	Height to Minimum Dilution ( $z_m / l_b$ )	Height to Top of Plume ( $z_e / l_b$ )	Plume Thickness ( $h_e / l_b$ )
F0	0	-1.54%	20.43%	29.52%	18.71%
F01	0.1	15.46%	13.86%	2.69%	35.58%
F1	1	-1.44%	-15.61%	-19.41%	-4.70%
F10	10	-0.27%	0.22%	-19.74%	-17.56%
F100	100	-12.13%	-42.48%	-21.62%	-22.28%

Table 3.1: Percent difference between ROMS simulation data and closest RSB series 3 and 4 experiments. Negative percentages indicate underprediction and positive percentages indicate overprediction.

Table 3.1 shows quantitative comparisons of ROMS experiments to RSB validation data. Generally, minimum dilution is well predicted while more variance is observed in plume rise height. Top of plume height percent divergence converges to approximately 20% for  $F \geq 1$ .

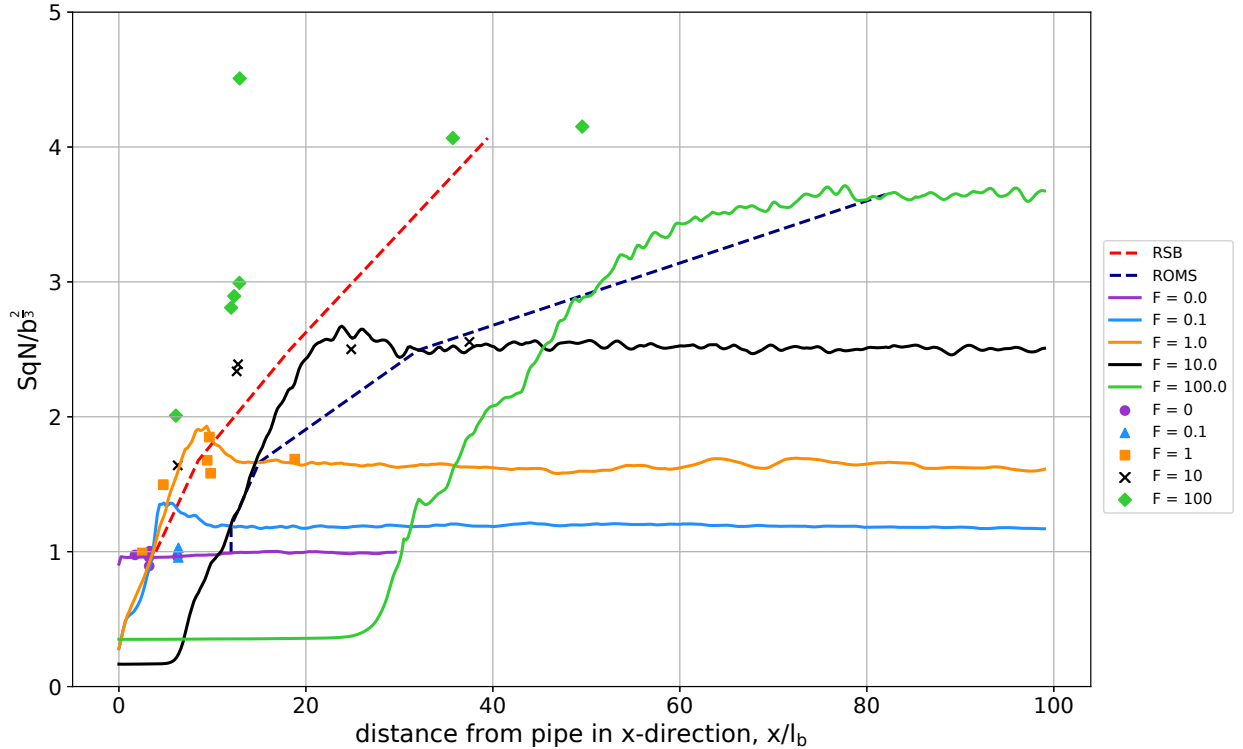


Figure 3.2: Minimum dilutions for each Froude number at normalized distances away from the pipe. Solid lines are ROMS experiments for each Froude number. Symbols are RSB experiments, and red dashed line is Equation 3.1 representing location of established wastefield in RSB experiments. Navy dashed line intersects points of established wastefield in ROMS experiments.

Disparity at  $F = 100$  is most egregious and is addressed in Section 3.2. The largest deviation between ROMS and RSB experiments is 42% and the smallest is less than 1%.

Figure 3.2 shows ROMS nondimensional dilution versus length results (solid line), plotted with RSB experimental data (symbols) for various Froude. Colors indicate different  $F$  experiments. The experiments increase in dilution as the effluent is pushed away from the pipe and mixed by ambient forcing until reaching a nearly constant dilution. Good agreement is observed in low Froude number flows ( $\leq 10$ ), and the trend of increasing dilution with Froude number is present. However, at high velocities ( $F = 100$ ), the high-resolution ROMS substantially underpredicts dilution while low velocities show a slight overprediction of dilution. Roberts et al., 1989b defines the established wastefield as the end of the initial

mixing region  $x_i$ , which is the distance to the point where the limiting value of dilution is obtained. The red dashed line in Figure 3.2 signifies the location of established wastefield of the RSB laboratory experiments given in Roberts et al., 1989b as a function of  $F$

$$\frac{x_i}{l_b} = 8.5F^{1/3} \quad (3.1)$$

Quantification of the established wastefield for minimum dilution and height parameters are taken at this point in the analyses of Roberts et al., 1989a.

The buoyant plumes in Froude numbers 0.1 and 1 are still developing at the intersection with the dashed line. An overshoot of the dilution of the emerging plume is apparent followed by additional mixing to a depressed dilution in  $F = 0.1, 1$ , and 10. Dilution increase during plume development near the pipe may be an artifact of the parameterized effluent forcing. Uniform mixing of the effluent at the input may overestimate near field initial dilution. Some experimental data coincides with the overshoot in  $F = 1$ . For Froude numbers 10 and 100, the distance required before the plume becomes established is longer and does not intersect. Contrary to Roberts et al., 1989a, dilution is affected by current and  $F = 0.1$  is not equal to the dilution at  $F = 0$ .

The established wastefield location of Roberts et al., 1989a experiments do not match for the ROMS experiment and the correct distance away from the pipe for the established wastefield must be determined. Figure 3.2 is used to visually determine the end of the initial mixing region after initial plume development. The locations after the overshoot of dilution are chosen. The established wastefield locations for  $F = 0, 0.1, 1, 10$ , and 100 are  $x/l_b = 12, 12, 15, 32$ , and 82, respectively. The navy dashed curve in Figure 3.2 represents these points and their corresponding dilution. These locations are used to represent the established wastefield for this metric and other metrics that will be described,  $z_m, z_e$ , and  $h_e$ . In Figure 3.2, the maximum  $x/l_b$  is 100 for  $F \geq 0.1$ , which corresponds to 1300 meters away from the pipe, because the wastefield dilutions are unchanging after that point bar minor perturbations and to better highlight the area closer to the pipe.

Figure 3.3 shows normalized minimum dilution in the established wastefield as a function of Froude number. Minimum dilution values are taken at the  $x/l_b$  values listed above. Lower

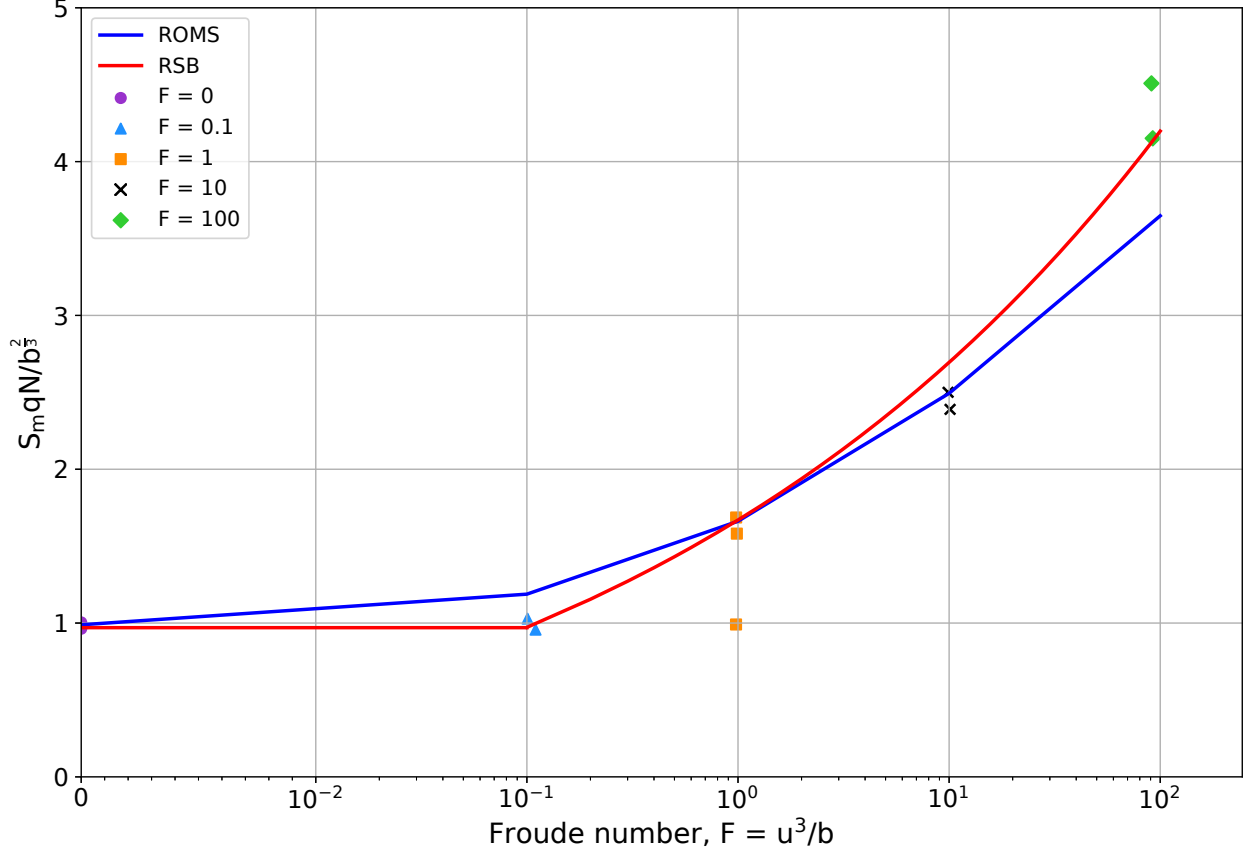


Figure 3.3: Normalized minimum dilution in the established wastefield for each Froude number.

dilution is observed for  $F = 100$  and higher dilution for low  $F$  than experimental data. Note that the scale of the x-axis of  $F$  on all graphs is linear from 0 to  $10^{-2}$  and logarithmic for  $> 10^{-2}$ . Symbols represent RSB experimental data for minimum dilution at the established wastefield (Roberts et al., 1989c). Red curves plotted in Figure 3.3 are dilution data fit curves as a function of Froude number presented in Roberts et al., 1989a:

$$\frac{S_m q N}{b^{2/3}} = 0.97, \quad F \leq 0.1 \quad (3.2)$$

and

$$\frac{S_m q N}{b^{2/3}} = 2.19F^{1/6} - 0.52, \quad 0.1 < F \leq 100 \quad (3.3)$$

The higher dilutions in the ROMS experiments for  $F = 0.1$  in both Figures 3.2 and 3.3 suggest additional mixing may be occurring in ROMS that is not present in the laboratory

experiments. Parameterized initial mixing of effluent during input into the model may be the cause of additional dilution. Minimum dilutions for Froude numbers 1 and 10 match nearly exactly with the observed dilutions in the experiments. Note that the data fit curve, Equation 3.3, overestimates the  $F = 10$  data points.

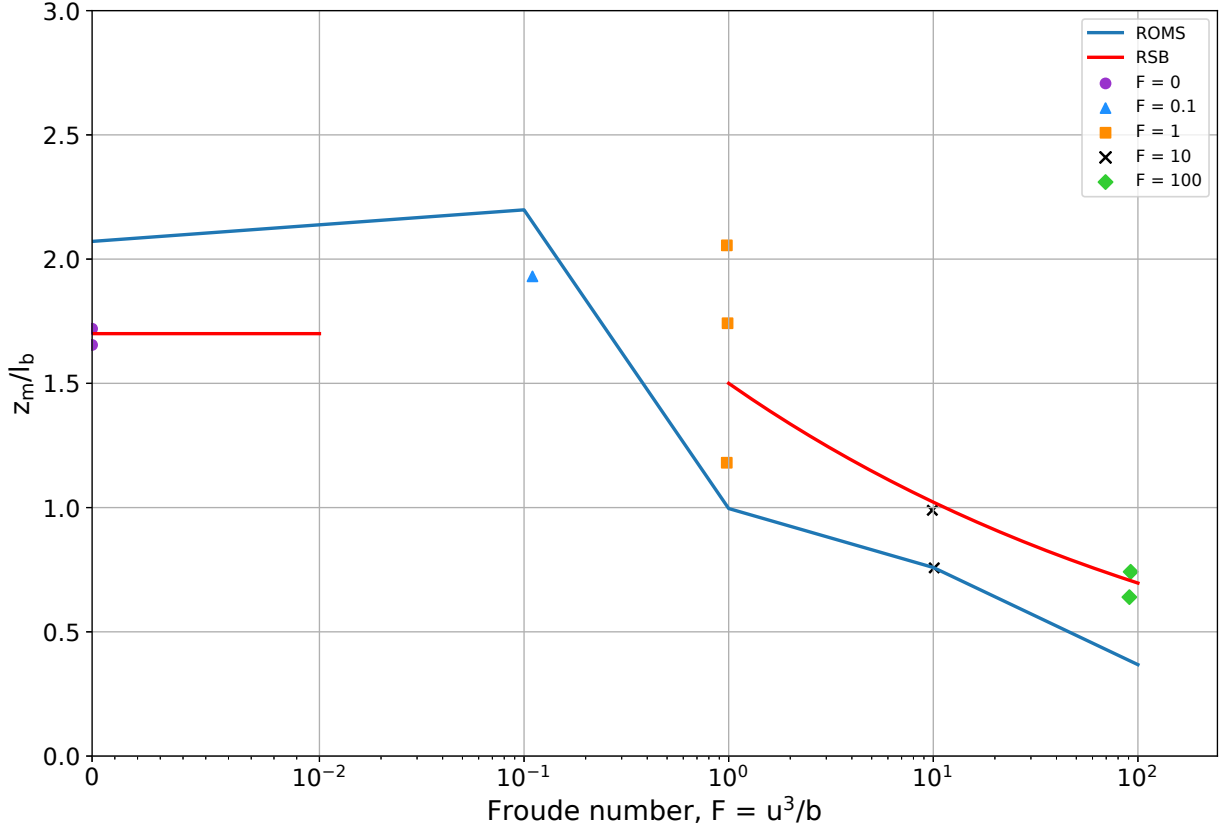


Figure 3.4: Normalized height to minimum dilution in the established wastefield for each Froude number.

The vertical plume characteristics of rise height to minimum dilution,  $z_m$ , top of the plume,  $z_e$ , and thickness,  $h_e$ , at the end of the initial mixing region are found for all experiments. To determine  $z_e$  and  $h_e$ , Roberts et al., 1989a found the heights where the concentrations are 5% of the maximum concentration. The same method is employed here.

Height to minimum dilution,  $z_m$ , or height to maximum concentration, at the established wastefield shown in Figure 3.4 reveals a similar overprediction for lower Froude numbers and under prediction for  $F = 100$  as the dilution metrics. The RSB empirical equations plotted

are Eq. 16c,

$$\frac{z_m}{l_b} = 1.7, \quad F \leq 0.1 \quad (3.4)$$

and Eq. 18,

$$\frac{z_m}{l_b} = 1.5F^{-1/6}, \quad 0.1 < F \leq 100 \quad (3.5)$$

in Roberts et al., 1989a. Minimum dilution height at the end of the initial mixing region changes by 6% between  $F = 0$  and 0.1. Between  $F = 0$  and 0.1 in the RSB experiments, the change is 11% and 15% for the two data points. The height of the Froude number 0 case between ROMS and RSB is overestimated by 20% and 25%. Although dilution has good agreement in Figures 3.2 and 3.3 for  $F = 1$ , the height to the minimum dilution is underestimated by 15% for the lowest data point.  $F = 10$  matches the closest to the experiment while  $F = 100$  shows the largest deviation from RSB experiments out of all metrics at 42%.

Normalized height to top of the plume is plotted against Froude number in Figure 3.5 and normalized thickness of the plume is plotted in Figure 3.6. The equations Eq. 16a, 16b,

$$\frac{z_e}{l_b} = 2.6; \quad \frac{h_e}{l_b} = 1.8, \quad F \leq 0.1 \quad (3.6)$$

and Eq. 17

$$\frac{z_e}{l_b}, \frac{h_e}{l_b} = 2.5F^{-1/6}, \quad 0.1 < F \leq 100 \quad (3.7)$$

from Roberts et al., 1989a are plotted on the Figures 3.5 and 3.6.

Froude number 0.1 ROMS simulation height to top of the plume is consistent with experimental data. However, other model data lacks agreement.  $F = 0$  overpredicts top of the plume by nearly 30% and  $F > 0.1$  underpredicts by 20% or more.

Despite good agreement of  $z_e$  for  $F = 0.1$ , the difference between experimental and model  $h_e$  is one of the largest deviations at 35%, indicating the bottom of the plume is not well represented. Figure 3.1(b) shows a thick plume of about 35 meters between 100 and 700 meters away from the pipe, and the plume thickness decreases further away. The increased dilution is likely contributing to the increased plume thickness as well.  $F = 1$  underpredicts the top and minimum dilution of the plume but is close to the laboratory experiments for

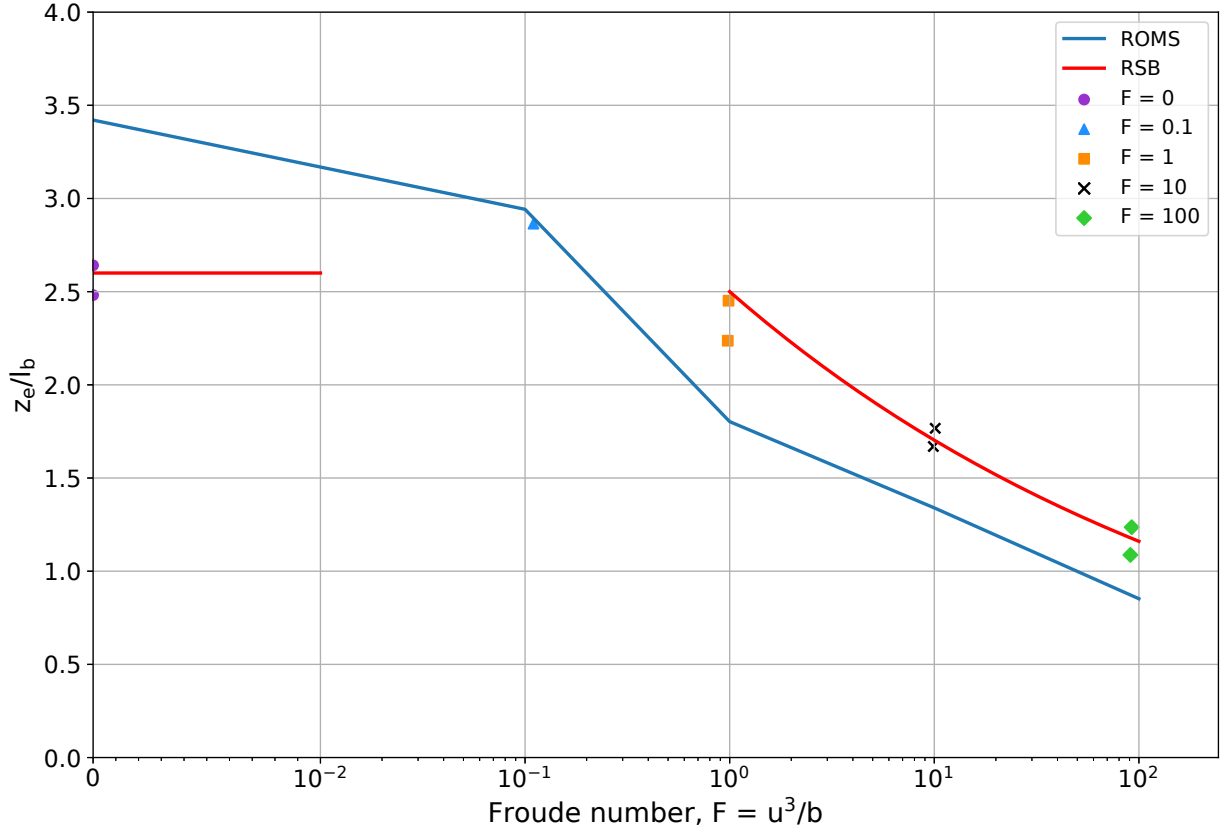


Figure 3.5: Height to top of the established wastefield, defined as 5% of maximum concentration, for each Froude number.

plume thickness. This indicates that  $z_m$  and  $z_e$  are underestimated by similar heights and gives nearly the expected plume thickness. The  $z_e$  and  $h_e$  are virtually the same as each other for  $F = 10$  and  $100$  due to the forced entrainment plume regime.

Minimum dilution heights plotted against distances away from the pipe are presented in Figure 3.7. Roberts et al., 1989a,b,c does not plot this relationship, but it is included here for analysis. For Froude numbers 0.1 and 1, the height to maximum concentration changes substantially over distance after the end of the initial mixing region. The other Froude numbers have little change after reaching the established wastefield. This could indicate the intermediate field plays a large role at  $F = 0.1$  and  $1$  for  $z_m$ . The dissimilarity between the RSB experimental data and model data is apparent. The differences of  $x$  in dilution and  $z_m$  are compounded here to give large deviations.

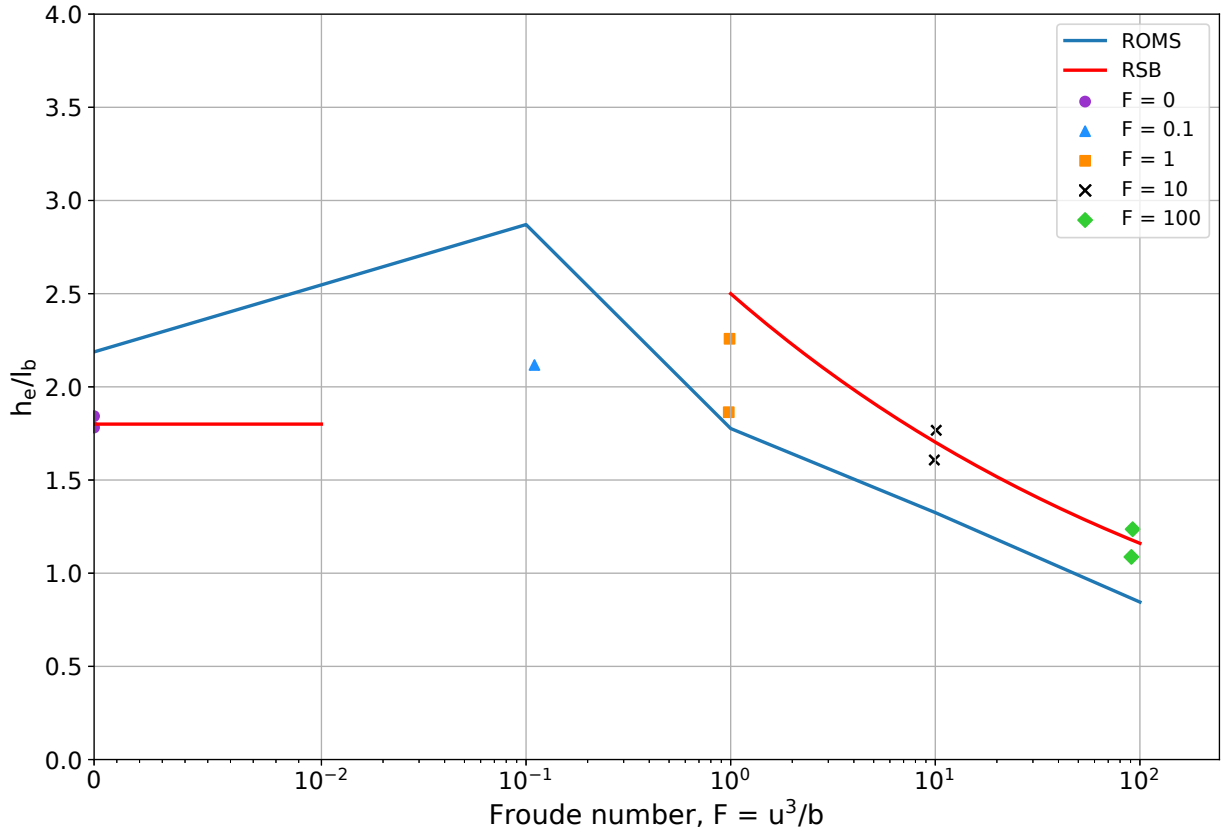


Figure 3.6: Thickness of the established wastefield, defined as 5% of maximum concentration, for each Froude number.

Froude number 1 has a strong signal of an internal wave between fluid layers called a lee wave (Figure 3.1(c)). Lee waves are generated from stably stratified flow over an obstacle, with the obstacle here consisting of the constant intrusion of a buoyant plume, and oscillate at the Brunt-Väisälä frequency (Marshall and Plumb, 2008). Roberts et al., 1989a also noted a resemblance of a pronounced internal wave in their  $F = 1$  experiments. Internal wave propagation is more accurately predicted in nonhydrostatic than hydrostatic (Guillaume et al., 2017). The internal wave propagation in plume is apparent in oscillating features in  $F = 1$  in Figures 3.1 and 3.7.

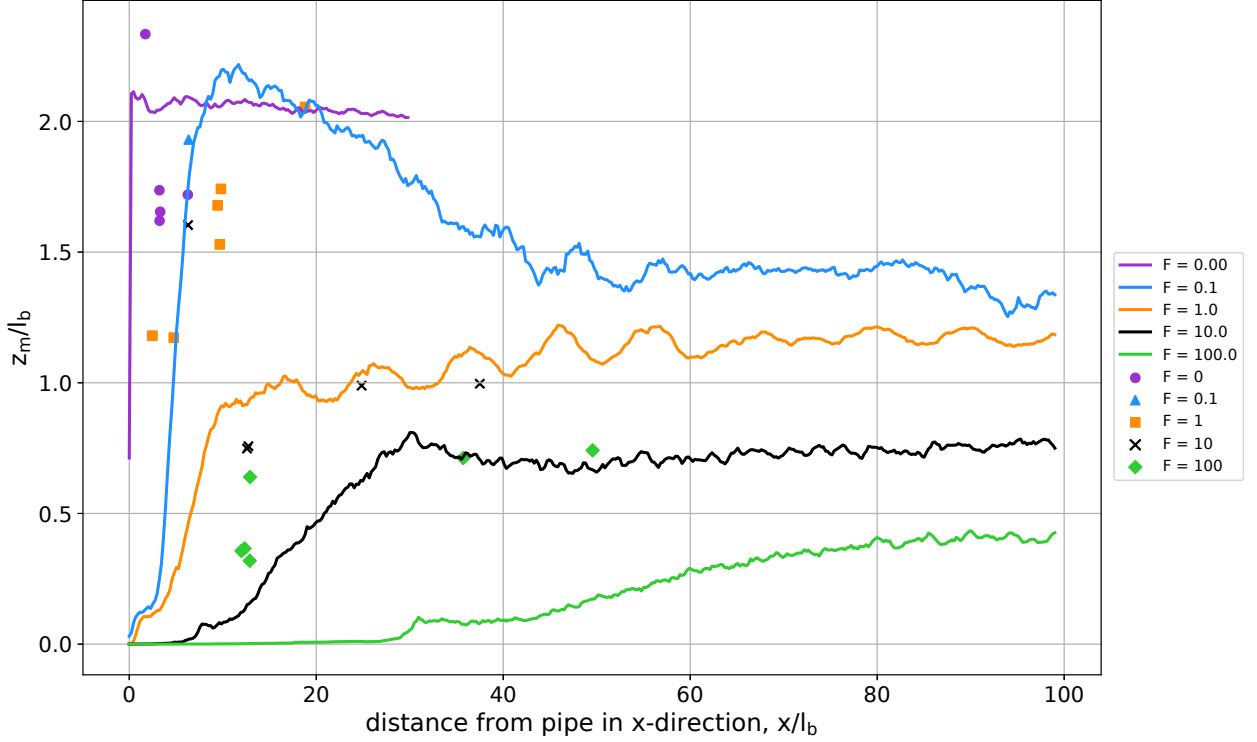


Figure 3.7: Height to minimum dilution at normalized distances away from the pipe. This metric was not presented by Roberts et al., 1989a,b,c.

### 3.2 Sensitivity to resolution

Spanning spatio-temporal scales is computationally challenging. A spatial resolution accurately resolving intermediate plume dynamics, while retaining computational efficiency is desirable. Three resolutions are tested in the Froude number 100 case at 10 m, 3 m and 1 m. Results are presented in Figures 3.8 – 3.13.

We seek to better resolve the Froude number 100 case by two methods: increase the spatial resolution to 1 m and shrink the source width of the pipe from 30 m to 15 m. A lower resolution of 10 m is also used to compare the effect of resolution. The 1 m resolution run has a shorter pipe length because the grid dimensions are fixed. The maximum length of the pipe with the 1024 by 512 grid is 512 m. A 500 m length pipe was chosen to prevent unwanted boundary interactions, and the volume flux was reduced proportionally to  $5.55556 \text{ m}^3 \text{ s}^{-1}$ . The sponge layer width is reduced to 33 meters in the 1 meter simulation. The 10 m

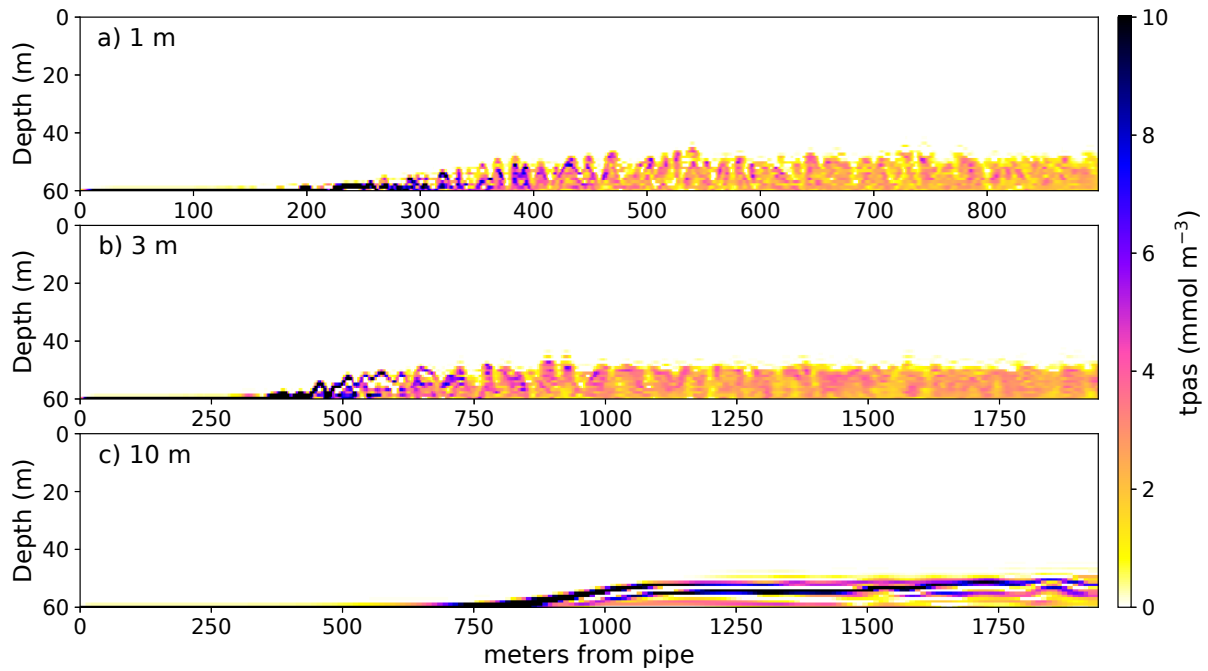


Figure 3.8: Snapshots of passive tracer at (a) 1 m resolution, (b) 3 m resolution, and (c) 10 m resolution with  $F = 100$  at the center of the pipe length and after 11.75 hours of model time. Note different  $x$ -scale for (a) compared to (b) and (c).

run was run on a smaller grid of 256 by 128 to capture the same area as the 1 m resolution for comparison and decrease computing time. Vertical resolution was kept at 64 grid points in a 60 meter vertical domain regardless of horizontal resolution.

Figure 3.8 shows ROMS model instantaneous fields at 1 m, 3 m, and 10 m resolution simulations. The domain of the 1 m simulation (Figure 3.8(a)) is too small to compare to the 10 m (c) and therefore only the 3 m (b) and 10 m (c) have the same  $x$ -scale. More vertical variation is apparent in the 1 m run than the 3 m. Less homogeneity of the plume structure and additional gaps of plume are present in (a) as a result of more resolved small-scale mixing. The 10 m experiment (c) clearly does not resolve plume dynamics at this Froude number. The 10 m plume has rigid, smooth structure without vertical protuberance that is uncharacteristic of plume structures. The forced entrainment regime is present in all resolutions, but the intermediate mixing and advection and diffusion vary for each resolution. Numerical diffusion from the upstream advection scheme decreases with grid scale (Uchiyama

et al., 2014).

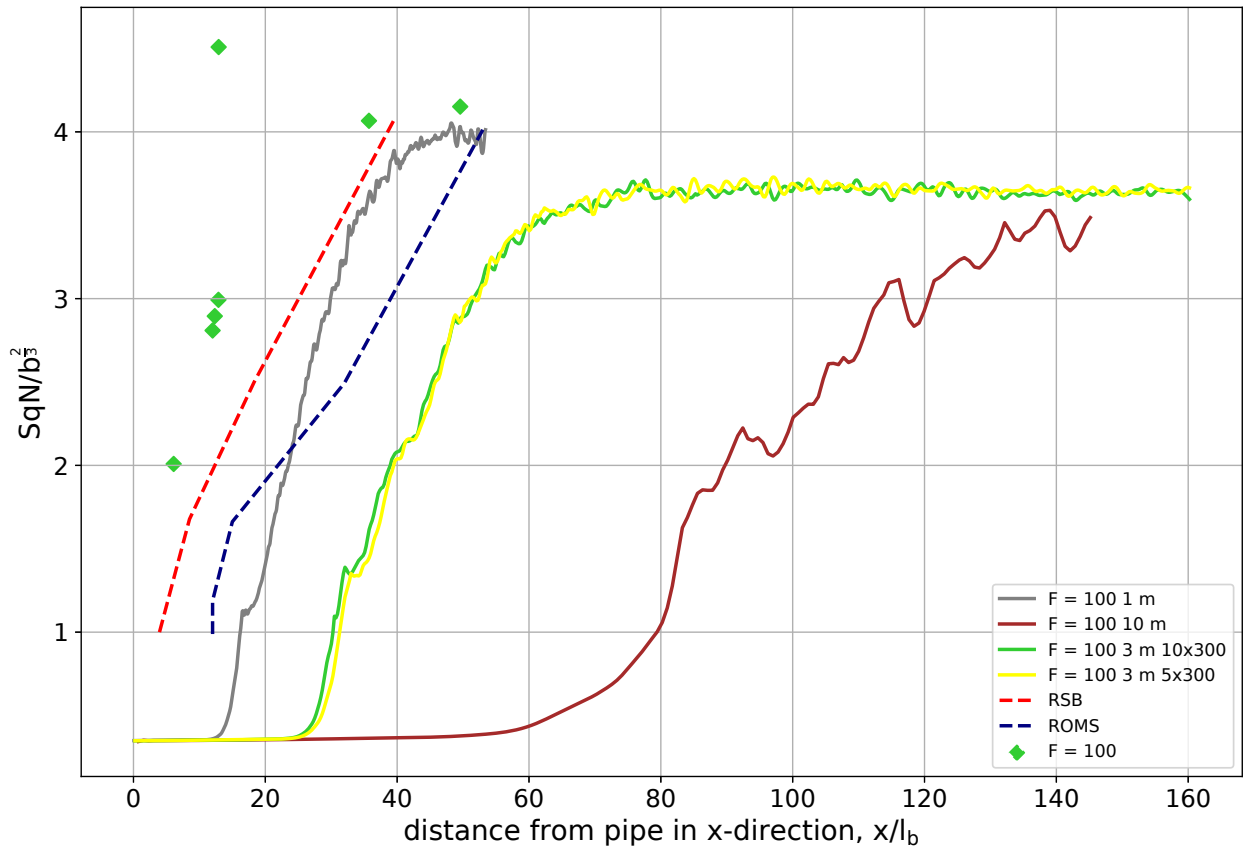


Figure 3.9: As 3.2, minimum dilutions over distance away from the pipe with solely Froude number 100 experiments with original 3 m resolution, 1 m resolution (gray), 10 m resolution (brown), and halved pipe source width (yellow). Navy dashed line is updated ROMS established wastefield curve with dilution in the 1 m resolution.

Figure 3.9 reveals that resolution plays a dramatic role in dilution at  $F = 100$ . The plume develops and rises in less distance and has higher minimum dilutions at the 1 m resolution compared to other resolutions. The navy dashed line, representing the location of established wastefield, matches more closely with the RSB established wastefield curve (red dashed curve). Decreasing source width and thereby increasing source volume flux plays no role in dilution change over distance in the 3 meter resolution experiments. It is apparent intermediate field processes are not well resolved at 10 m resolution. The 10 m plume takes more than 500 meters before rising off the first grid cell in the vertical domain and whether

the plume has reached the state of established wastefield is unclear.

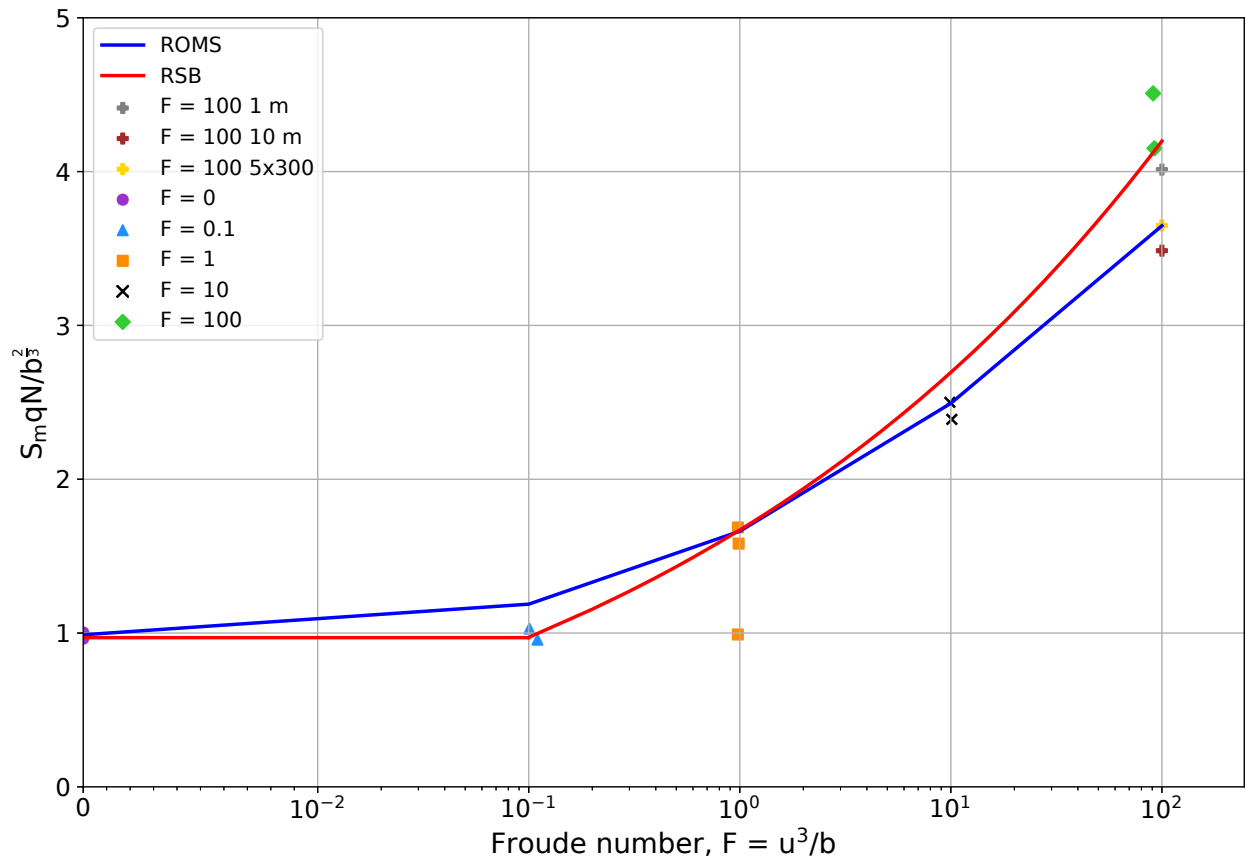


Figure 3.10: As Figure 3.3, minimum dilution in the established wastefield for each Froude number at different resolutions for  $F = 100$  experiments. Gray symbol represents 1 m resolution run, brown symbol represents 10 m resolution, and yellow represents smaller source width.

Figure 3.10 shows the minimum dilution plotted against the Froude number with inclusion of different resolution experiments. Symbols at  $F = 100$  represent the respective color resolution simulations. The locations of the end of the initial mixing region for 1 m and 10 m resolutions are  $x/l_b = 53$  and  $x/l_b = 145$ , respectively. Dilution nearly reaches the RSB experimental value in the 1 m resolution for  $F = 100$  in Figure 3.10. The 1 m resolution case increases dilution by 0.36 normalized units in the established wastefield compared to the 3 m resolution. The smaller pipe width has no change in the minimum dilution at the end of the initial mixing region. The 10 m simulation has the lowest dilution although the

location of established wastefield is more than 1500 meters away from the pipe.

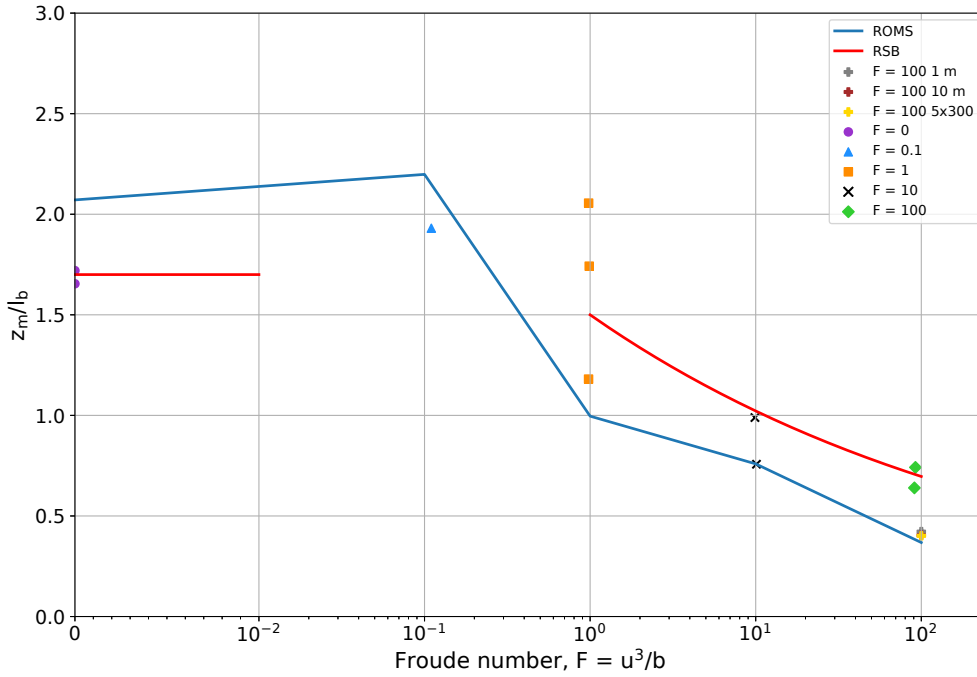


Figure 3.11: As Figure 3.4, height to minimum dilution in the established wastefield for each Froude number.

Height to normalized minimum dilution, shown in Figure 3.11, increased by 0.05, corresponding to 0.65 m rise, in the 1 m resolution compared to the 3 m resolution, or by 15%. The smaller pipe width increased marginally and can be attributed to being within the variance. Less dilution should lead to higher plume rise as seen by increasing Froude number, yet the lower dilution of the 10 m simulation leads to the same minimum dilution height as the smaller pipe width experiment. The difference in dilution between the 3 m and 10 m may be too small to observe a change in height.

Figures 3.12 and 3.13, as discussed previously, show that  $z_e$  and  $h_e$  are the same at  $F = 100$  because the plume stays at the bottom of the vertical domain. The height to top and thickness of plume increases by 0.074, corresponding to a 0.97 meter increase, for the 1 m resolution. The smaller pipe width and 10 m resolution have the same  $z_e$  and  $h_e$  as the original 3 m resolution. The 1 m resolution simulation clearly shows better agreement with the RSB experiments at  $F = 100$ .

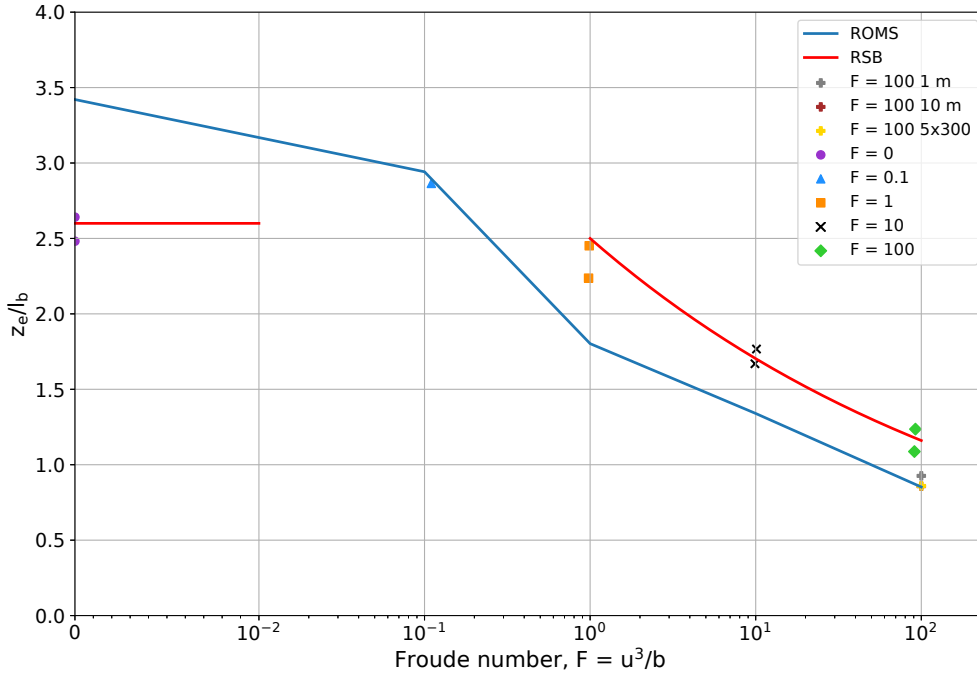


Figure 3.12: Height to top of the established wastefield, defined as 5% of maximum concentration, for each Froude number including additional  $F = 100$  simulations.

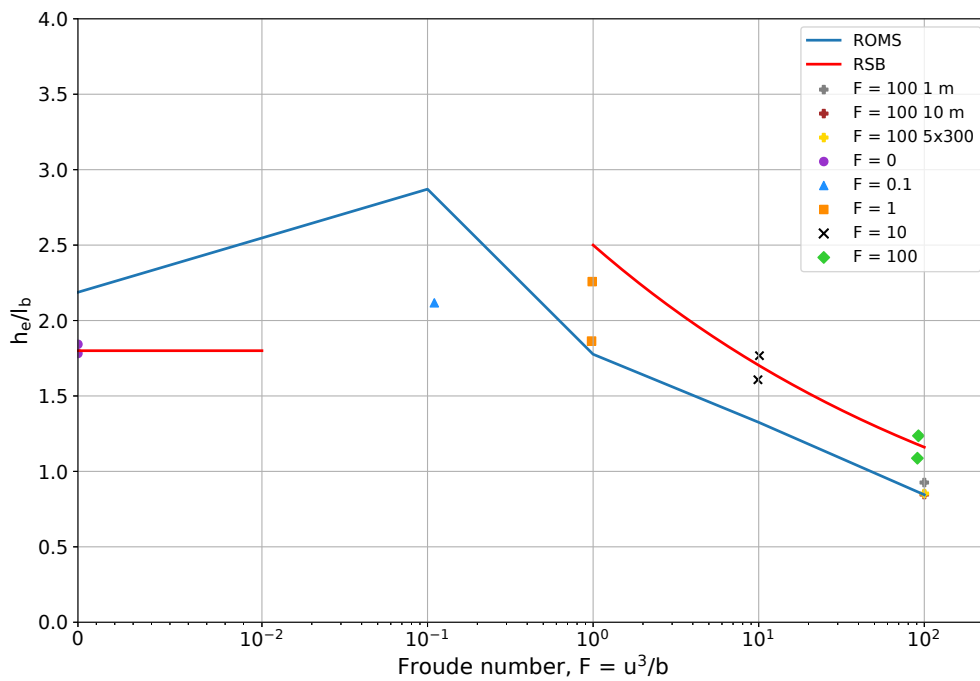


Figure 3.13: Thickness of the established wastefield, defined as 5% of maximum concentration, for each Froude number including additional  $F = 100$  ROMS experiments.

### 3.3 Sensitivity to time step

Results at high Froude numbers varied with time step because of numerical instability that did not violate the CFL condition.

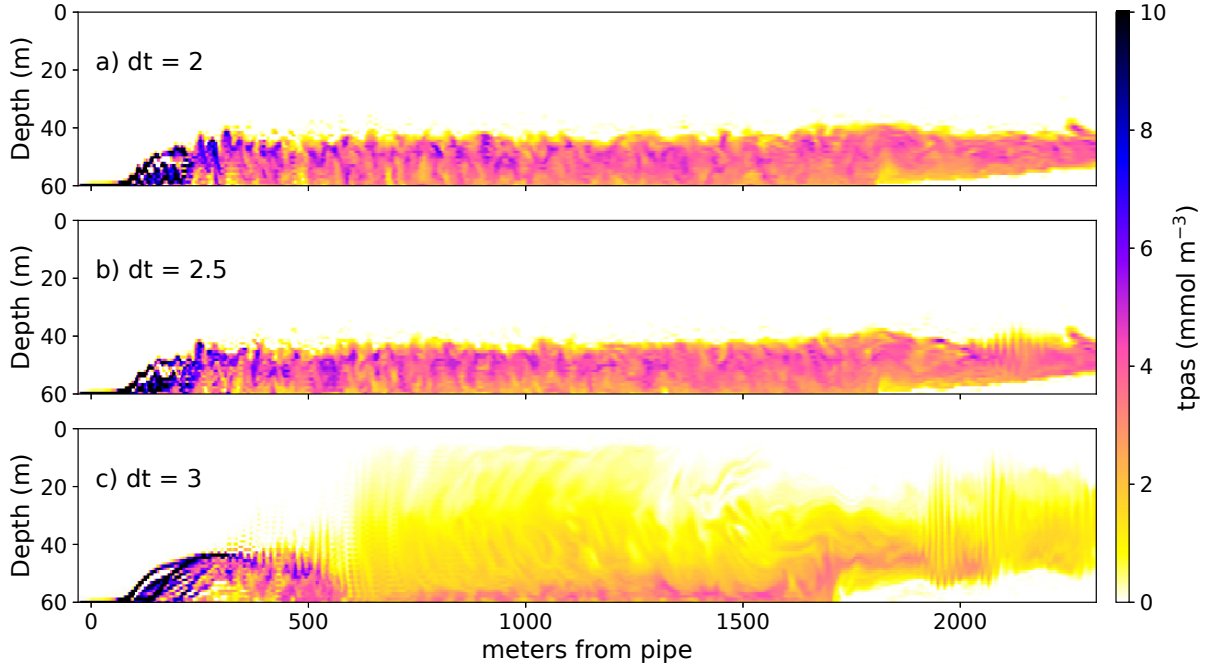


Figure 3.14: Instantaneous fields of passive tracer in  $F = 10$  experiments with time steps of 2, 2.5, and 3 seconds after 2.25 hours of simulation time. Snapshot is taken at the middle of the length of the pipe.

Figure 3.14 shows snapshots of  $F = 10$  experiments with passive tracer and time steps of 2, 2.5, and 3 seconds after 2.25 hours of simulation time. A time step of 2 seconds has no noticeable instabilities on the top of the plume. Time step 2.5 seconds has hints of instability ripples about 2100 m away from the pipe at the top of the plume, suggesting that this simulation is on the precipice of becoming unstable. Numerical instabilities are apparent in the  $F = 10$  simulation with a time step value of 3 seconds. Pillars of plume entrain into the water column at grid size scale and cause massive turbulence and mixing.

Froude number 10 experiments with different time steps are plotted on Figure 3.15 examining vertical profiles of  $w$ ,  $u$ , and passive tracer concentration. Metrics are averaged over

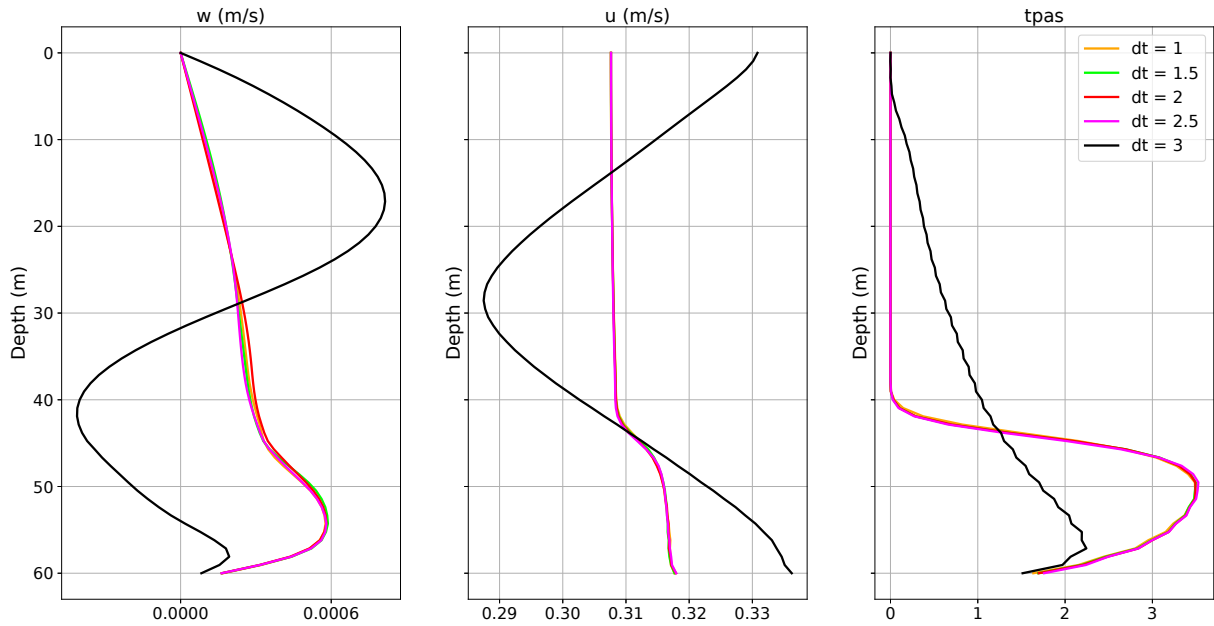


Figure 3.15: Vertical profiles of Froude number 10 experiments at different time steps examining  $w$ ,  $u$ , and passive tracer concentration with time steps in seconds. Note that  $dt = 1$ , 1.5, 2, and 2.5 profile lines are on top of each other

the length of the pipe and between 1.2 and 2.1 kilometers away from the pipe to focus on areas of instability in the established wastefield. Time steps 1 to 2.5 seconds converge at all depths. A time step value of 3 seconds shows higher velocity magnitudes in  $w$  and  $u$ . The shape of the  $u$  vertical profile indicates high velocity shears are occurring. Subtracting the cross flow velocity of  $F = 10$ , which is  $0.31013 \text{ m s}^{-1}$ , a net negative velocity forms in the middle of the water column sandwiched by positive velocities above and below. The resultant phenomenon is strong velocity shear at the transitional depths between net positive and net negative velocity, causing turbulence and mixing. The passive tracer then can be highly diluted from this instituted turbulence, and the effluent is mixed throughout the water column to nearly the surface. Plotting the  $F = 10$  3 second time step results with the RSB validation gave dilutions that were as high as  $F = 100$  dilutions. Despite time step convergence between 1 and 2.5 seconds, 2.5 seconds showed signs of instability as seen from the snapshot in Figure 3.14.

The CFL condition for this experiment is given as

$$\frac{u\Delta t}{\Delta x} = \frac{0.31013 \cdot 3 \text{ m s}^{-1} \cdot \text{s}}{3 \text{ m}} = 0.31013 < 0.5 \quad (3.8)$$

General CFL guidelines suggest CFL number should be less than 0.5. The CFL condition is met in this run, and the model does not abort. The cause of this numerical instability is hypothesized to be that the internal wave phase speed is greater than what can be resolved at the time step of 3 seconds and is explored in Section 4.4.

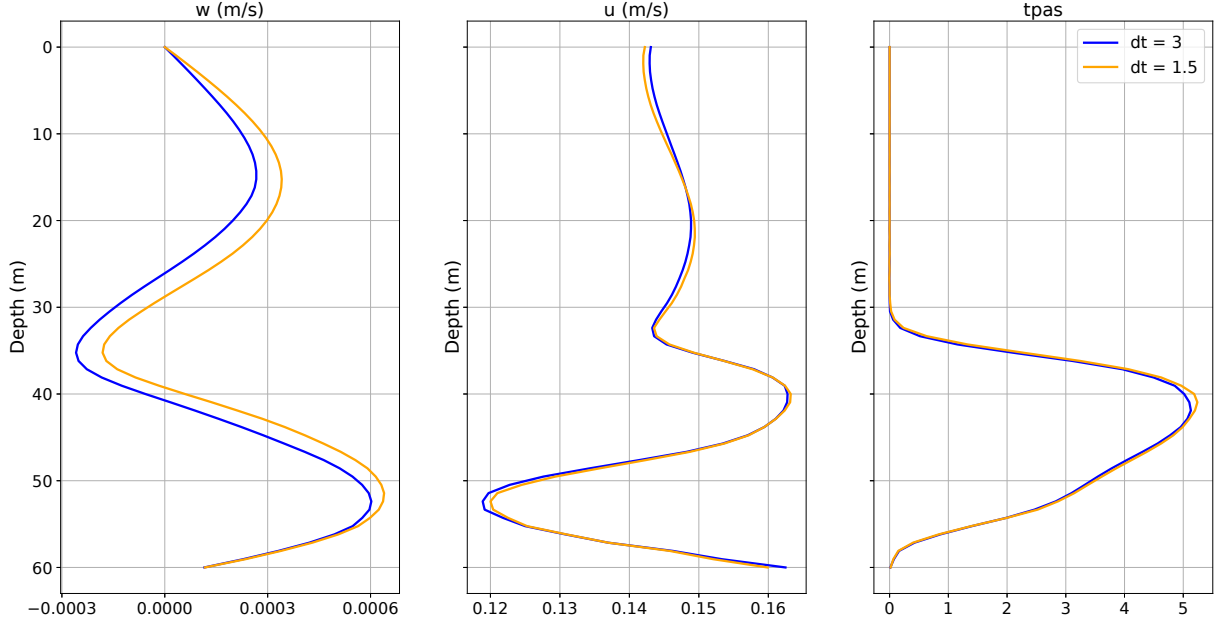


Figure 3.16: Comparison of different time stepping values for  $F = 1$  case of vertical velocity  $w$ , cross flow velocity  $u$ , and passive tracer concentration  $tpas$  vertical profiles averaged over length of the pipe and 700 – 1.3 km away from the pipe.

A lower time step was tested at  $F = 1$  to determine whether the strong internal wave is a result of a numerical instability and compared in Figure 3.16. The  $w$ ,  $u$ , and passive tracer concentration are compared at time steps 1.5 and 3 seconds averaged over the length of the pipe and between 700 and 1300 meters away from the pipe. A difference of less than  $10^{-4}$  is found in vertical velocity at each depth. Profiles of eastward velocity and passive tracer concentration are nearly identical.

Figure 3.17 reveals strong, alternating positive and negative vertical velocities above the pipe at time steps 3 and 1.5 seconds. The velocities are regimented near the pipe and

dissipate further from the pipe. Figure 3.1(c) supports this observation with clear internal waves of effluent at the top of the plume and near the pipe. Patterns of vertical velocity are nearly identical between the two time steps across the vertical and horizontal domains. From these metrics, it can be determined that  $F = 1$  internal waves do not occur because of numerical instabilities.

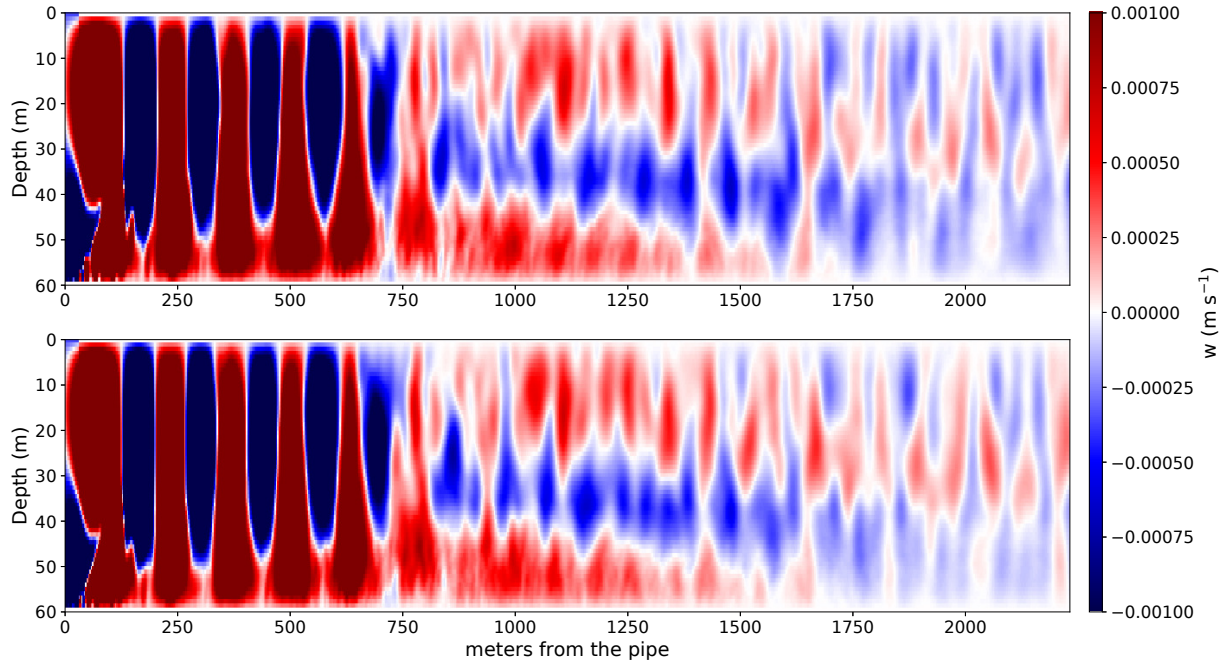


Figure 3.17: Vertical velocities comparison of  $F = 1$  simulations at different time steps averaged in along pipe distance and over the first 5.75 hours. Top plot is  $dt = 3$  seconds and bottom is  $dt = 1.5$  seconds.

# CHAPTER 4

## Discussion

### 4.1 Minimum Dilution Height

ROMS underpredicts top of the plume and minimum dilution heights for high Froude number experiments despite close agreement in dilution. To determine the cause of the underprediction, a simple approach to calculating the level of neutral density the plume reaches is considered:

$$\begin{aligned} d &= \frac{\max(c(z))}{c_{\text{inc}}} \\ \rho_{\text{mix}} &= \frac{\rho_a + \rho_e d}{1 + d} \end{aligned} \tag{4.1}$$

where  $d$  is dilution ratio,  $\max(c(z))$  is maximum concentration in the water column,  $c_{\text{inc}}$  is the incoming passive tracer concentration of  $1500 \text{ mmol m}^{-3}$ ,  $\rho_{\text{mix}}$  is the resultant mixed density,  $\rho_a$  is the ambient density at the discharge point, and  $\rho_e$  is the density of effluent. This metric assumes additional mixing after parameterized effluent input does not occur and rise height is simply a function of initial source dilution. The reason for this analysis is to deduce the importance of parameterized initial mixing at the bottom.  $\max(c(z))$  is calculated from the minimum dilution, or maximum concentration, at the established wastefield for each Froude number. The values used for  $\max(c(z))$  here are the maximum concentrations used to calculate the plotted values in Figure 3.3. The normalized values plotted on Figure 3.3 for  $F = 0, 0.1, 1, 10, \text{ and } 100$  are  $S_m q N / b^{2/3} = 0.989, 1.188, 1.662, 2.493, 3.648$  and correspond to the  $\max(c(z))$  of  $8.946, 7.446, 5.322, 3.547, 2.425 \text{ mmol m}^{-3}$ , respectively, by reversing the dilution and normalization calculations. This method calculates the neutral density the plume reaches with the assumption that all mixing occurs at the input cell, or bottom cell. The neutral density is then approximated to a height based on the initial ambient density

profile in Figure 2.4. The  $z_m/l_b$  can be calculated for this analysis from the approximated height.

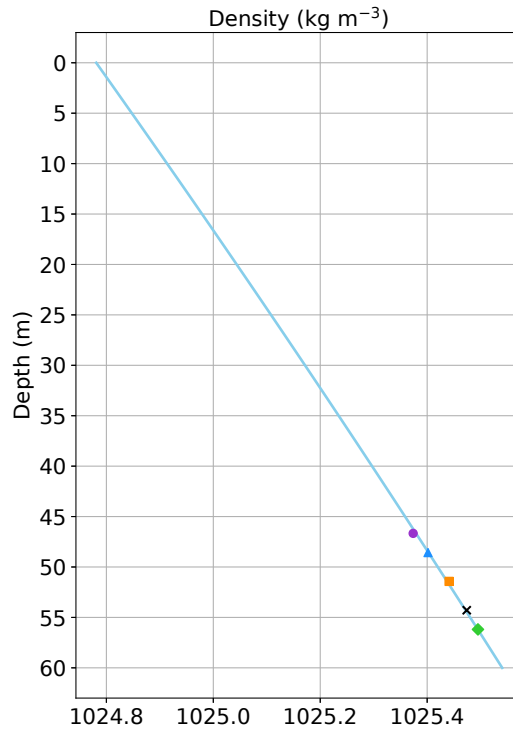


Figure 4.1: Simple density calculation to determine height in meters to neutral buoyancy. Blue line is initial ambient density profile from Figure 2.4, and symbols represent the height to neutral buoyancy of minimum dilution for each Froude number experiment.

The results of this approach are plotted in Figure 4.1 in meters. The corresponding  $z_m/l_b$  for  $F = 0, 0.1, 1, 10,$  and  $100$  are  $1.019, 0.873, 0.655, 0.437,$  and  $0.291,$  respectively. Comparatively, the ROMS  $z_m/l_b$  values from Figure 3.4 are  $2.071, 2.198, 0.996, 0.759,$  and  $0.368$  from low to high Froude number. The height to minimum dilution is substantially underpredicted compared to the ROMS results in Figure 3.4. Additional mixing and diffusion occurs as the plume rises through the water column in the intermediate field. The parameterization of uniform mixing at effluent input does not solely determine the rise height. Notably, the parameterized effluent input mixing contributes to plume rise height underprediction in the ROMS simulations. The 1 m resolution results show higher dilution and rise height of plume minimum and top of the plume, yet does not reach the values of the RSB laboratory

experiments (Figures 3.9 – 3.13). This may be attributed to overmixing (i.e., less buoyant in the initial input of effluent). The relationship between dilution and plume rise depends on where mixing occurs. Mixing primarily at the bottom in cold, dense water leads to lower plume height because the plume density is increased. If less mixing occurs at the bottom and more is mixed in the intermediate field higher in the water column, the density becomes lower (i.e., more buoyant), and the plume rises higher. Increasing resolution to accurately resolve near field mixing will likely resolve this issue. Additionally, parameterizing effluent forcing input for given Froude numbers may also give better approximations.

## 4.2 Realistic Stratification

The issue of uniform mixing at the effluent input is compounded with the ambient linearly stratified density profile in these simulations. In the ocean where effluent pipes are likely to be placed, vertical density gradients are less stratified than linear profiles. The strongest stratification is at the thermocline, where temperature decreases rapidly in relatively little depth. Elsewhere, the density gradients are minimal, especially in winter. A realistic ocean vertical profile has limited density differences between the bottom and thermocline. The overestimation of mixing at the bottom in these ROMS simulations is consequently less damaging in realistic ocean conditions.

A single profile of observations provided from a CTD instrument near the OCSD pipe is plotted with the average of all available wintertime observation profiles within a 3 by 3 km area of the pipe and the linear profile used in these experiments in Figure 4.2. The single profile is an instantaneous measurement of the water column.

The density anomaly from the bottom to the surface of the water is  $0.14 \text{ kg m}^{-3}$  in the observation profile. The linearly stratified density profile has a density anomaly of  $0.76 \text{ kg m}^{-3}$ . The density difference is striking. Equation 4.1 is used to calculate the rise of height in the single observation profiles with the same dilutions of the ROMS simulations. Figure 4.3 reveals that a plume discharging into ambient conditions of the single observation profile rises much higher than in a linear stratified water column. The minimum dilution heights of low

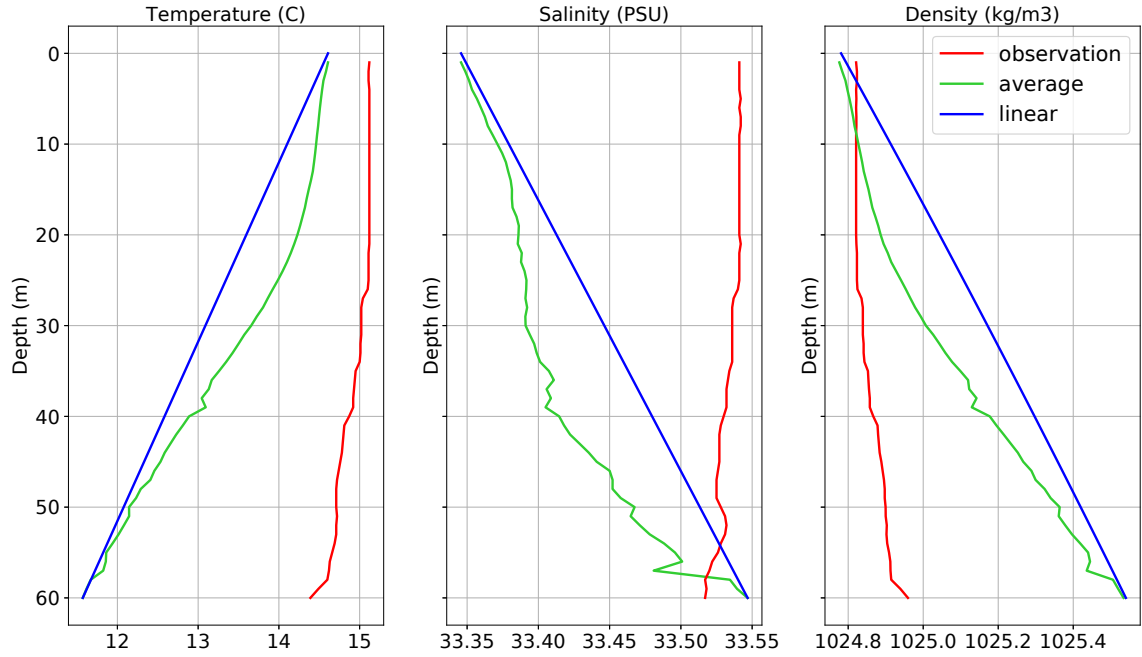


Figure 4.2: Observed ocean profile from CTD instrument measurement (red) plotted next to the average of all observation profiles within a 3 by 3 km area of the pipe (green) the linear profile (blue) used in these ROMS simulations.

Froude numbers reach the surface of the water column and heights for  $F = 1$  and 10 increase by 10 meters. The  $F = 100$  increases by a smaller height of 2 meters and corresponds to  $z_m/l_b = 0.438$ . The similarity of the  $z_m/l_b$  to the linear stratification case indicates that the forced entrainment regime and high velocity in  $F = 100$  dominate for minimum dilution height regardless of ambient density.

Within the average profile of Figure 4.2, the density gradient is even stronger near the bottom than the linear profile and becomes weaker near the surface. An average profile poorly resolves average conditions in the SCB. Additionally, ocean conditions that are uniform horizontally are unlikely to occur. Profiles of temperature and salinity, and therefore density, change over distance.

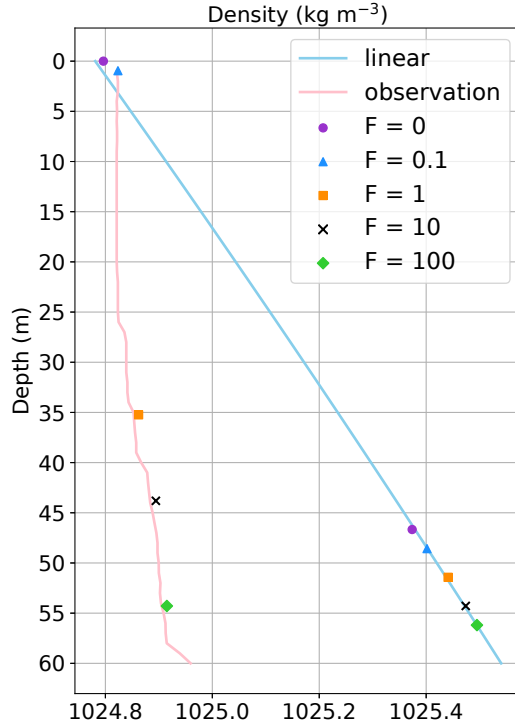


Figure 4.3: Neutral density calculation comparing linear and single observation profile.

### 4.3 Resolution

High velocity flows agreement with experimental results was not achieved in these experiments. The ROMS experiments require more distance away from the pipe to reach the established wastefield for high Froude numbers, but the intermediate process seems well represented to reach the established wastefield. The sensitivity to resolution results indicate that high velocity ambient flows require higher resolution to account for the processes behind high dilution and mixing. Low Froude numbers also benefit from higher resolution to minimize parameterized effluent input. The end dilutions and plume height characteristics for 3 m and 10 m simulations are similar. This may imply the vertical resolution is more important for these parameters than the horizontal. The distance required before the 10 m simulation reaches an established wastefield is substantially overestimated and indicates that different effluent input parameterization must be used at lower resolution.

## 4.4 High Froude Number Instability

The source of numerical instability at high Froude numbers is speculated as an inability to resolve internal wave phase speed at given time steps. A rough estimation of internal wave phase speed in constant stratification can be given as

$$u_p = (N \cdot H) + u \quad (4.2)$$

where  $u_p$  is the phase speed,  $N$  is the Brunt-Väisälä frequency,  $H$  is the height of the vertical domain, and  $u$  is the ambient current. This equation is a simplification of general wave phase velocity  $v_p = \omega\lambda/2\pi$ , where  $\omega$  is the angular frequency and  $\lambda$  is the wavelength.  $\lambda/2\pi$  is approximated to equal the height of the domain. For internal waves,  $\omega = N\cos\theta$ , where  $\theta$  is the angle between wave vector and horizontal plane and is assumed to be zero (Pedlosky, 2003).  $u_p = 0.96995 \text{ m s}^{-1}$  given  $N = 0.010997 \text{ s}^{-1}$ ,  $H = 60 \text{ m}$ , and  $u = 0.31013 \text{ m s}^{-1}$ . The CFL number using  $u_p$  becomes 0.96995 with time step 3 seconds and exceeds 0.5. With time step 2 seconds, CFL number is 0.64663. Although this CFL number also exceeds 0.5, this crude method of approximating phase speed helps elucidate the difference in CFL number and time step stability of the model. A full analysis of the cause of the instability is beyond the scope of this work and explored in future work.

## CHAPTER 5

### Conclusions and Future Work

A high-resolution, nonhydrostatic version of ROMS with wastewater pipe was developed and tested against laboratory experiments of varying cross flow Froude numbers. Three meter resolution experiments accurately predict buoyant plume flow regime and reasonably predict dilution metrics for low cross flow Froude numbers. When cross flow velocity is high (e.g.,  $F > 1$ ) simulations require more down pipe distance for accurate plume development. Internal wave structure in the buoyant plume of  $F = 1$  is present.  $F = 100$  underpredicts minimum dilution at three meter spatial resolution. One meter resolution simulations produce more accurate results; however, the results are slightly biased compared to laboratory collected data suggesting that near field dynamics (i.e.,  $< 1$  m) are fundamental to plume resolution. This bias may suggest that ultra high-resolution simulations ( $\sim 10$  cm) are required to fully resolve initial mixing or, alternatively, parameterization is required to empirically simulate the initial mixing zone (e.g., initialize plume higher in the water column). Greater concurrence of dilution and height parameters is expected with higher resolution for all Froude numbers. Height parameters of  $z_m$ ,  $z_e$ , and  $h_e$  are generally overpredicted for low  $F$  and underpredicted for high  $F$ . Despite lack of convergence of horizontal resolution for dilution and height parameters in high Froude numbers, reasonable success is achieved at Froude numbers in typical SCB oceanic conditions. Examination of various time stepping results suggest numerical instability without CFL criterion violation and warrant further research.

This model can be used to prescribe effluent properties and range of dilution for appropriate plume dispersion and rise height to minimize coastal impacts. Current regulation for wastewater treatment plants rely on measurement data and empirical and jet integral models

to meet permit requirements. Plume measurements have been difficult to capture because of their transient nature and current models require many approximations without the full context of plume development and intermediate field dynamics. Three-dimensional numerical models resolving multiple spatio-temporal scales can be informative and prognostic for wastewater management. Local wastewater discharge impact on chemistry and ecology can be assessed by development and integration of a biogeochemical module. Impact of effluent concentration increases, seasonal ocean conditions, and intermittent effluent flow on dilution and rise of height can be easily assessed. Wastewater plume tracking from sufficient observation data may be possible. Critically, accurate simulation facilitates prescribed effluent density and volume flux to prevent deleterious plume effects.

Applications of this high-resolution nonhydrostatic ROMS model are abundant. Increasing resolution to a centimetric level facilitates accurate simulation of near field dynamics. Realistic domains with varying bathymetry, nonuniform flows, atmospheric forcing, tides, and Earth's rotation can alter buoyant plume fate and transport. High-resolution, nested simulations allow near, intermediate, and far field to be well represented. Future work includes refined initial mixing parameterizations and increasing resolution to capture and observe near field dynamics with eventual goal of nested modeling using realistic, regional scale domains with complete atmospheric and oceanic forcing.

## Bibliography

Ai, J., A. W.-K. Law, and S. C. M. Yu

2006. On boussinesq and non-boussinesq starting forced plumes. *Journal of Fluid Mechanics*, 558:357386. 13

Ai, J. J., S. C. M. Yu, A. W.-K. Law, and L. P. Chua

2005. Vortex dynamics in starting square water jets. *Physics of Fluids*, 17(1):014106. 13

Anderson, D. M.

1997. Turning back the harmful red tide. *Nature*, 388:513–514. 2

Arakawa, A. and V. Lamb

1977. Methods of computational physics. *New York: Academic Press*, 17:173–265. 19

Bleninger, T. and G. Jirka

2004. Near-and far-field model coupling methodology for wastewater discharges. *Environmental hydraulics and sustainable water management*, Pp. 447–453. 9

Blumberg, A. F., Z.-G. Ji, and C. K. Ziegler

1996. Modeling outfall plume behavior using far field circulation model. *Journal of hydraulic engineering*, 122(11):610–616. 14, 17

Blumberg, A. F. and G. L. Mellor

1987. A description of a three-dimensional coastal ocean circulation model. *Three-dimensional coastal ocean models*, Pp. 1–16. 14

Botelho, D., I. Teakle, M. Barnes, M. Barry, R. Baheerathan, G. Shiell, and G. Collocut

2016. Linking nearfield cfd models of buoyant discharges to far field dispersion models. In *Proceedings of International Symposium on Outfall Systems. Ottawa, Canada University of Ottawa*. 18

Bouma, T., L. Van Duren, S. Temmerman, T. Claverie, A. Blanco-Garcia, T. Ysebaert, and

P. Herman

2007. Spatial flow and sedimentation patterns within patches of epibenthic structures: Combining field, flume and modelling experiments. *Continental Shelf Research*, 27(8):1020–1045. 14

Carvalho, J. L. B., P. J. W. Roberts, and J. Roldo

2002. Field observations of ipanema beach outfall. *Journal of Hydraulic Engineering*, 128(2):151–160. 4, 9, 12

Cederwall, K.

1971. Buoyant slot jets into stagnant or flowing environments. Technical Report KH-R-25, W. M. Keck Laboratory of Hydraulics and Water Resources, California Institute of Technology. 32

Choi, K. W. and J. H. Lee

2007. Distributed entrainment sink approach for modeling mixing and transport in the intermediate field. *Journal of Hydraulic Engineering*, 133(7):804–815. 9, 13, 17, 18

Conley, D. J., H. W. Paerl, R. W. Howarth, D. F. Boesch, S. P. Seitzinger, K. E. Havens, C. Lancelot, and G. E. Likens

2009. Controlling eutrophication: Nitrogen and phosphorus. *Science*, 323(5917):1014–1015. 1

Courant, R., K. Friedrichs, and H. Lewy

1967. On the partial difference equations of mathematical physics. *IBM Journal of Research and Development*, 11(2):215–234. 28

Dalkey, A. and J. F. Shisko

1996. Observations of oceanic processes and water quality following seven years of ctd surveys in santa monica bay, california. *Bulletin of the Southern California Academy of Sciences*, 95. 3

Dauhajre, D. P., J. C. McWilliams, and Y. Uchiyama

2017. Submesoscale coherent structures on the continental shelf. *Journal of Physical Oceanography*, 47(12):2949–2976. 19
- Doneker, R. L. and G. H. Jirka  
 1991. Expert systems for mixing zone analysis and design of pollutant discharges. *Journal of Water Resources Planning and Management*, 117(6):679–697. 9
- Doneker, R. L. and G. H. Jirka  
 2001. Cormix-gi systems for mixing zone analysis of brine wastewater disposal. *Desalination*, 139(1):263 – 274. 9, 13
- Ernst, G. G. J., R. S. J. Sparks, S. N. Carey, and M. I. Bursik  
 1996. Sedimentation from turbulent jets and plumes. *Journal of Geophysical Research: Solid Earth*, 101(B3):5575–5589. 6
- Fischer, H. B., J. E. List, C. R. Koh, J. Imberger, and N. H. Brooks  
 1979. *Mixing in Inland and Coastal Waters*. New York: Academic Press. 3, 5, 6
- Frick, W., P. Roberts, L. Davis, J. Keyes, D. Baumgartner, and K. George  
 2003. Dilution models for effluent discharges. *Visual Plumes, EPA/600/R-03*, 25. 5, 6, 11, 12
- Frick, W. E.  
 1984. Non-empirical closure of the plume equations. *Atmospheric Environment (1967)*, 18(4):653 – 662. 10, 11
- Frick, W. E.  
 2004. Visual plumes mixing zone modeling software. *Environmental Modelling & Software*, 19(7):645 – 654. Facilitating Constructive Government-Industry Interactions. 5, 10, 13
- Frick, W. E., D. J. Baumgartner, and C. G. Fox  
 1994. Improved prediction of bending plumes. *Journal of Hydraulic Research*, 32(6):935–950. vi, 10, 11

Gierach, M. M., B. Holt, R. Trinh, B. J. Pan, and C. Rains

2017. Satellite detection of wastewater diversion plumes in southern california. *Estuarine, Coastal and Shelf Science*, 186:171 – 182. Tracking impacts of anthropogenic nutrient inputs in an urban coastal ecosystem during a wastewater diversion in the southern California bight. 3

Gourbesville, P. and B. Thomassin

2000. Coastal environment assessment procedure for sustainable wastewater management in tropical islands: the mayotte example. *Ocean Coastal Management*, 43(12):997 – 1014. 16

Guillaume, R., M. M. Jeroen, D. Nicolas, and D. Thomas

2017. Compact symmetric poisson equation discretization for non-hydrostatic sigma coordinates ocean model. *Ocean Modelling*, 118:107 – 117. 22, 41

Gula, J., M. J. Molemaker, and J. C. McWilliams

2015. Gulf stream dynamics along the southeastern u.s. seaboard. *Journal of Physical Oceanography*, 45(3):690–715. 19

Haidvogel, D., H. Arango, W. Budgell, B. Cornuelle, E. Curchitser, E. D. Lorenzo, K. Fennel, W. Geyer, A. Hermann, L. Lanerolle, J. Levin, J. McWilliams, A. Miller, A. Moore, T. Powell, A. Shchepetkin, C. Sherwood, R. Signell, J. Warner, and J. Wilkin

2008. Ocean forecasting in terrain-following coordinates: Formulation and skill assessment of the regional ocean modeling system. *Journal of Computational Physics*, 227(7):3595 – 3624. Predicting weather, climate and extreme events. 19, 20

Howard, M. D. A., M. Sutula, D. A. Caron, Y. Chao, J. D. Farrara, H. Frenzel, B. Jones, G. Robertson, K. McLaughlin, and A. Sengupta

2014. Anthropogenic nutrient sources rival natural sources on small scales in the coastal waters of the southern california bight. *Limnology and Oceanography*, 59(1):285–297. 1, 19

Hunt, G. R. and N. G. Kaye

2001. Virtual origin correction for lazy turbulent plumes. *Journal of Fluid Mechanics*, 435:377396. 13

Israelsson, P. H., Y. D. Kim, and E. E. Adams

2006. A comparison of three lagrangian approaches for extending near field mixing calculations. *Environmental Modelling Software*, 21(12):1631 – 1649. 5, 14

Jirka, G.

2004. Integral model for turbulent buoyant jets in unbounded stratified flows. Part I: Single round jet. *ENVIRONMENTAL FLUID MECHANICS*, 4(1):1–56. 8

Jirka, G. H., G. Abraham, and D. R. F. Harleman

1975. An assessment of techniques for hydrothermal prediction. Technical report. vi, 4

Jones, B., A. Bratkovich, T. Dickey, G. Kleppel, A. Steele, R. Iturriaga, and I. Haydock

1990. Variability of physical, chemical, and biological parameters in the vicinity of an ocean outfall plume. In *Stratified flows*, Pp. 877–890. ASCE. 3

Kanarska, Y., A. Shchepetkin, and J. McWilliams

2007. Algorithm for non-hydrostatic dynamics in the regional oceanic modeling system. *Ocean Modelling*, 18(3):143 – 174. 20, 21, 22

Kang, S.-W., B.-C. Oh, K.-S. Park, and S.-H. You

1999. Near-field dilution of wastewater effluents discharged from submerged ocean outfalls in masan bay. *KSCE Journal of Civil Engineering*, 3(4):395–405. 9

Kim, Y.-D., S.-W. Kang, I.-W. Seo, and B.-C. Oh

2000. Far-field transport of effluent plumes discharged from masan sea outfalls. *Ocean and Polar Research*, 22(2):69–80. 14

Kim, Y. D., I. W. Seo, S. W. Kang, and B. C. Oh

2001. Modeling the mixing of wastewater effluent discharged from ocean outfalls using a hybrid model. *Coastal Engineering Journal*, 43(4):259–288. 14, 17, 23

Kim, Y. D., I. W. Seo, S. W. Kang, and B. C. Oh

2002. Jet integral particle tracking hybrid model for single buoyant jets. *Journal of Hydraulic Engineering*, 128(8):753–760. vi, 14, 17

Koh, R. C. and N. H. Brooks

1975. Fluid mechanics of waste-water disposal in the ocean. *Annual Review of Fluid Mechanics*, 7(1):187–211. vi, 2, 3

Konstantinidou, K. and P. N. Papanicolaou

2003. Vertical round and orthogonal buoyant jets in a linear density-stratified fluid. In *Proc. 30th IAHR Congress on Water Engineering and Research in a Learning Society: Modern Developments and Traditional Concepts*, Pp. 293–300. 6

LACSD

2019. Los angeles county sanitation district water reclamation. <https://www.lacsd.org/wastewater/wwfacilities/moresanj.asp>. Online, accessed: 2019-08-06. 3, 4

Large, W. G., J. C. McWilliams, and S. C. Doney

1994. Oceanic vertical mixing: A review and a model with a nonlocal boundary layer parameterization. *Reviews of Geophysics*, 32(4):363–403. 19

Lee, J. H. W. and V. Cheung

1990. Generalized lagrangian model for buoyant jets in current. *Journal of Environmental Engineering*, 116(6):1085–1106. 9

Lee, J. H.-w. and V. Chu

2012. *Turbulent jets and plumes: a Lagrangian approach*. Springer Science & Business Media. 9

Lesser, G., J. Roelvink, J. van Kester, and G. Stelling

2004. Development and validation of a three-dimensional morphological model. *Coastal Engineering*, 51(8):883 – 915. Coastal Morphodynamic Modeling. 16, 17

Lewis, R. et al.

1997. *Dispersion in estuaries and coastal waters*. Chichester: John Wiley & Sons. 5

Lyon, G. S. and E. D. Stein

2008. How effective has the clean water act been at reducing pollutant mass emissions to the southern california bight over the past 35years? *Environmental Monitoring and Assessment*, 154(1):413. 1

Marchesiello, P., J. C. McWilliams, and A. Shchepetkin

2003. Equilibrium structure and dynamics of the california current system. *Journal of Physical Oceanography*, 33(4):753–783. 19

Marshall, J. and R. A. Plumb

2008. *Atmosphere, ocean and climate dynamics: an introductory text*, volume 93. Academic Press. 41

Matos, J., A. Monteiro, P. Costa, R. Neves, A. Bettencourt, A. Frazao, and C. Santos

1998. Wastewater diffusion in the estoril coast: Theoretical calculations and field studies. *Water Science and Technology*, 38(10):337 – 344. Water Quality International '98. 9

McLaughlin, K., N. P. Nezlin, M. D. Howard, C. D. Beck, R. M. Kudela, M. J. Mengel, and G. L. Robertson

2017. Rapid nitrification of wastewater ammonium near coastal ocean outfalls, southern california, usa. *Estuarine, Coastal and Shelf Science*, 186:263 – 275. in Tracking impacts of anthropogenic nutrient inputs in an urban coastal ecosystem during a wastewater diversion in the southern California bight. 1

McWilliams, J. C.

2006. *Fundamentals of geophysical fluid dynamics*. Cambridge University Press. 21

Mirajkar, H. N. and S. Balasubramanian

2017. Effects of varying ambient stratification strengths on the dynamics of a turbulent buoyant plume. *Journal of Hydraulic Engineering*, 143(7):04017013. 6

- Mirajkar, H. N., S. Tirodkar, and S. Balasubramanian  
 2015. Experimental study on growth and spread of dispersed particle-laden plume in a linearly stratified environment. *Environmental Fluid Mechanics*, 15(6):1241–1262. 6
- Moharir, R. V., K. Khairnar, and W. N. Paunikar  
 2014. Mike 3 as a modeling tool for flow characterization: A review of applications on water bodies. *International Journal of Advanced Studies in Computers, Science and Engineering*, 3(3):32. 16
- Molemaker, M. J., J. C. McWilliams, and W. K. Dewar  
 2015. Submesoscale instability and generation of mesoscale anticyclones near a separation of the california undercurrent. *Journal of Physical Oceanography*, 45(3):613–629. 19
- Morelissen, R., T. van der Kaaij, and T. Bleninger  
 2013. Dynamic coupling of near field and far field models for simulating effluent discharges. *Water Science and Technology*, 67(10):2210–2220. 15, 17
- Morton, B. R., G. I. Taylor, and J. S. Turner  
 1956. Turbulent gravitational convection from maintained and instantaneous sources. *Proceedings of the Royal Society of London. Series A. Mathematical and Physical Sciences*, 234(1196):1–23. 6, 8, 11, 22
- Muellenhoff, W., A. Soldate, D. Baumgartner, M. Schuldt, L. Davis, and W. Frick  
 1985. Initial mixing characteristics of municipal ocean discharges. *Rep. No. EPA-600/3-85-073a*. 12
- Nekouee, N., S. A. Hamidi, P. J. W. Roberts, and D. J. Schwab  
 2015. Assessment of a 3d hydrostatic model (pom) in the near field of a buoyant river plume in lake michigan. *Water, Air, & Soil Pollution*, 226(7):210. 22
- Nezlin, N. P., M. A. Sutula, R. P. Stumpf, and A. Sengupta  
 2012. Phytoplankton blooms detected by seawifs along the central and southern california coast. *Journal of Geophysical Research: Oceans*, 117(C7). 1

Niu, H., K. Lee, T. Husain, B. Veitch, and N. Bose

2011. *A Coupled Model for Simulating the Dispersion of Produced Water in the Marine Environment*, Pp. 235–247. New York, NY: Springer New York. vi, 4, 16

OCSD

2019. Orange county water and sanitation district groundwater replenishment system. <https://www.ocwd.com/gwrs/>. Online, accessed: 2019-08-06. 3, 4

Okubo, A. and M. J. Karweit

1969. Diffusion from a continuous source in a uniform shear flow. *Limnology and Oceanography*, 14(4):514–520. 5

Pedlosky, J.

2003. *Waves in the ocean and atmosphere: introduction to wave dynamics*. Springer Science & Business Media. 57

Penven, P., V. Echevin, J. Pasapera, F. Colas, and J. Tam

2005. Average circulation, seasonal cycle, and mesoscale dynamics of the peru current system: A modeling approach. *Journal of Geophysical Research: Oceans*, 110(C10). 19

Periez, R. and A. Elliott

2002. A particle-tracking method for simulating the dispersion of non-conservative radionuclides in coastal waters. *Journal of Environmental Radioactivity*, 58(1):13 – 33. 14

Pritchard, D., G. Savidge, and B. Elsässer

2013. Coupled hydrodynamic and wastewater plume models of belfast lough, northern ireland: A predictive tool for future ecological studies. *Marine pollution bulletin*, 77(1-2):290–299. 15

Rasmussen, E., I. S. Hansen, A. Erichsen, D. Muhlenstein, and J. Dorge

2000. volume 43. WIT Press. 16

Reichardt, H.

1941. über eine neue theorie der freien turbulenz. *ZAMM - Journal of Applied Mathematics and Mechanics / Zeitschrift für Angewandte Mathematik und Mechanik*, 21(5):257–264. 8
- Riddle, A., E. Beling, and R. Murray-Smith
2001. Modelling the uncertainties in predicting produced water concentrations in the north sea. *Environmental Modelling Software*, 16(7):659 – 668. 5
- Roberts, P. J.
1991. Ocean outfalls. *Critical Reviews in Environmental Control*, 20(5-6):311–339. 14
- Roberts, P. J. W.
1999. Modeling mamala bay outfall plumes. ii: Far field. *Journal of Hydraulic Engineering*, 125(6):574–583. 17
- Roberts, P. J. W., C. D. Hunt, M. J. Mickelson, and X. Tian
2011. Field and model studies of the boston outfall. *Journal of Hydraulic Engineering*, 137(11):1415–1425. 5, 23
- Roberts, P. J. W., W. H. Snyder, and D. J. Baumgartner
- 1989a. Ocean outfalls. i: Submerged wastefield formation. *Journal of Hydraulic Engineering*, 115(1):1–25. vi, vii, 5, 6, 8, 18, 24, 25, 28, 32, 36, 37, 38, 39, 40, 41, 42
- Roberts, P. J. W., W. H. Snyder, and D. J. Baumgartner
- 1989b. Ocean outfalls. ii: Spatial evolution of submerged wastefield. *Journal of Hydraulic Engineering*, 115(1):26–48. vii, 5, 6, 18, 28, 35, 36, 40, 42
- Roberts, P. J. W., W. H. Snyder, and D. J. Baumgartner
- 1989c. Ocean outfalls. iii: Effect of diffuser design on submerged wastefield. *Journal of Hydraulic Engineering*, 115(1):49–70. vii, 6, 18, 37, 40, 42
- Robertson, G.
2018. Personal correspondence. 2, 5, 23, 24, 29

- Rogowski, P., E. Terrill, J. Thomas, L. Rosenfeld, and J. Largier  
 2014. Orange county sanitation district (ocsd) outfall diversion—summary report. *Final Report prepared for the Orange County Sanitation District*, P. 92. vi, 27
- Schiff, K., D. Greenstein, N. Dodder, and D. J. Gillett  
 2016. Southern california bight regional monitoring. *Regional Studies in Marine Science*, 4:34 – 46. US Monitoring Programs. 1
- Schiff, K. C., M. J. Allen, E. Y. Zeng, and S. M. Bay  
 2000. Southern california. *Marine Pollution Bulletin*, 41(1-6):76–93. 1
- Scholin, C. A., F. Gulland, G. J. Doucette, S. Benson, M. Busman, F. P. Chavez, J. Cordaro, R. DeLong, A. D. Vogelaere, J. Harvey, M. Haulena, K. Lefebvre, T. Lipscomb, S. Loscutoff, L. J. Lowenstine, R. M. III, P. E. Miller, W. A. McLellan, P. D. R. Moeller, C. L. Powell, T. Rowles, P. Silvagni, M. Silver, T. Spraker, V. Trainer, and F. M. V. Dolah  
 2000. Mortality of sea lions along the central california coast linked to a toxic diatom bloom. *Nature*, 403:80–84. 2
- Shchepetkin, A. F. and J. C. McWilliams  
 1998. Quasi-monotone advection schemes based on explicit locally adaptive dissipation. *Monthly Weather Review*, 126(6):1541–1580. 20
- Shchepetkin, A. F. and J. C. McWilliams  
 2003. A method for computing horizontal pressure-gradient force in an oceanic model with a nonaligned vertical coordinate. *Journal of Geophysical Research: Oceans*, 108(C3). 19, 20
- Shchepetkin, A. F. and J. C. McWilliams  
 2005. The regional oceanic modeling system (ROMS): a split-explicit, free-surface, topography-following-coordinate oceanic model. *Ocean Modelling*, 9(4):347 – 404. 19, 20
- Smith, J., P. Connell, R. H. Evans, A. G. Gellene, M. D. Howard, B. H. Jones, S. Kaveggia,

- L. Palmer, A. Schnetzer, B. N. Seegers, E. L. Seubert, A. O. Tatters, and D. A. Caron  
2018. A decade and a half of pseudo-nitzschia spp. and domoic acid along the coast of southern california. *Harmful Algae*, 79:87 – 104. Domoic acid 30 years on. 2
- Tomicic, B., A. Ltzen, and O. Mark  
2001. *Integrated Modelling of the Sewer System and the Receiving Waters for the Island of Ischia*, Pp. 548–557. 16
- Uchiyama, Y., E. Y. Idica, J. C. McWilliams, and K. D. Stolzenbach  
2014. Wastewater effluent dispersal in southern california bays. *Continental Shelf Research*, 76:36 – 52. 14, 15, 19, 20, 23, 25, 43
- Wang, H. and A. W.-K. Law  
2002. Second-order integral model for a round turbulent buoyant jet. *Journal of Fluid Mechanics*, 459:397428. 13
- Wang, R.-Q., A. W.-K. Law, E. E. Adams, and O. B. Fringer  
2011. Large-eddy simulation of starting buoyant jets. *Environmental Fluid Mechanics*, 11(6):591–609. 12, 13
- Warrick, J. A. and K. L. Farnsworth  
2017. Coastal river plumes: Collisions and coalescence. *Progress in Oceanography*, 151:245 – 260. 17
- Williams, R. G. and M. J. Follows  
2011. *Ocean dynamics and the carbon cycle: Principles and mechanisms*. Cambridge University Press. 21
- Wright, S. J., D. R. Wong, K. E. Zimmerman, and R. B. Wallace  
1982. Outfall diffuser behavior in stratified ambient fluid. *Journal of the Hydraulics Division*, 108(4):483–501. 3, 7
- Zhang, X.-Y. and E. E. Adams

1999. Prediction of near field plume characteristics using far field circulation model. *Journal of Hydraulic Engineering*, 125(3):233–241. 15, 17, 23

Zhao, L., Z. Chen, and K. Lee

2011. Modelling the dispersion of wastewater discharges from offshore outfalls: a review. *Environmental Reviews*, 19:107–120. 4, 6, 13, 14, 15, 22